

The relaxed-polar mechanism of locally optimal Cosserat rotations for an idealized nanoindentation and comparison with 3D-EBSD experiments

Andreas Fischle¹, Patrizio Neff², and Dierk Raabe³

June 16, 2018

Abstract

The rotation $\text{polar}(F) \in \text{SO}(3)$ arises as the unique orthogonal factor of the right polar decomposition $F = \text{polar}(F)U$ of a given invertible matrix $F \in \text{GL}^+(3)$. In the context of nonlinear elasticity Grioli (1940) discovered a geometric variational characterization of $\text{polar}(F)$ as a unique energy-minimizing rotation. In preceding works, we have analyzed a generalization of Grioli's variational approach with weights (material parameters) $\mu > 0$ and $\mu_c \geq 0$ (Grioli: $\mu = \mu_c$). The energy subject to minimization coincides with the Cosserat shear-stretch contribution arising in any geometrically nonlinear, isotropic and quadratic Cosserat continuum model formulated in the deformation gradient field $F := \nabla\varphi : \Omega \rightarrow \text{GL}^+(3)$ and the microrotation field $R : \Omega \rightarrow \text{SO}(3)$. The corresponding set of non-classical energy-minimizing rotations

$$\text{rpolar}_{\mu, \mu_c}^{\pm}(F) := \arg \min_{R \in \text{SO}(3)} \left\{ W_{\mu, \mu_c}(R; F) := \mu \left\| \text{sym}(R^T F - \mathbf{1}) \right\|^2 + \mu_c \left\| \text{skew}(R^T F - \mathbf{1}) \right\|^2 \right\}$$

represents a new *relaxed-polar* mechanism. Our goal is to motivate this mechanism by presenting it in a relevant setting. To this end, we explicitly construct a deformation mapping φ_{nano} which models an idealized nanoindentation and compare the corresponding optimal rotation patterns $\text{rpolar}_{1,0}^{\pm}(F_{\text{nano}})$ with experimentally obtained 3D-EBSD measurements of the disorientation angle of lattice rotations due to a nanoindentation in solid copper. We observe that the non-classical *relaxed-polar* mechanism can produce interesting counter-rotations. A possible link between Cosserat theory and finite multiplicative plasticity theory on small scales is also explored.

Key words: Cosserat, Cosserat couple modulus, Grioli's theorem, relaxed-polar mechanism, nanoindentation, 3D-EBSD, rotations, micropolar, non-symmetric stretch, counter-rotations.

AMS 2010: 15A24, 22E30, 74A30, 74A35, 74B20, 74E15, 74G65, 74N05, 74N15, 82D25.

¹Corresponding author: Andreas Fischle, Institut für Numerische Mathematik TU Dresden, Zellescher Weg 12-14, 01069 Dresden, Germany, email: andreas.fischle@tu-dresden.de
Dresden Center for Computational Materials Science (DCMS) (<http://dcms.tu-dresden.de/>)

²Patrizio Neff, Head of Lehrstuhl für Nichtlineare Analysis und Modellierung, Fakultät für Mathematik, Universität Duisburg-Essen, Thea-Leymann Str. 9, 45127 Essen, Germany, email: patrizio.neff@uni-due.de

³Dierk Raabe, Max-Planck-Institut für Eisenforschung, Max-Planck-Str. 1, 40237 Düsseldorf, Germany, email: d.raabe@mpie.de

Contents

1	Introduction	2
1.1	The locally energy-minimizing Cosserat rotations $\text{rpolar}_{\mu, \mu_c}^{\pm}(F)$	4
1.2	Geometric-mechanical aspects of optimal Cosserat rotations	5
2	Multiplicative plasticity, small elastic distortions and Cosserat theory	8
2.1	The strain energy density in isotropic multiplicative plasticity for negligible elastic strains	8
2.2	Symmetric best-approximation of the plastic stretch and complete spatial decoupling	10
2.3	Consistency of the modelling assumptions with the physics of a nanoindentation	11
3	Synthetic vs. experimental nanoindentation: a formal comparison	13
3.1	Nanoindentation in copper single crystals and 3D-EBSD analysis	13
3.2	Construction of a synthetic nanoindentation	16
3.3	Fields of energy-minimizing Cosserat rotations $\text{rpolar}_{1,0}^{\pm}(F)$	18
3.4	The planar spin as a measure for counter-rotations in a plane	19
3.5	A formal comparison of rotation patterns in experimental and synthetic nanoindentation	21
4	Conclusion	24
5	Acknowledgments	25
A	Supplementary Material	27
A.1	Best-approximation in $\text{Sym}^+(3)$ (due to Higham)	27
A.2	Algorithmic implementation of $\text{rpolar}_{1,0}^{\pm}(F)$	27

1 Introduction

We consider the weighted optimality problem for the Cosserat shear–stretch energy $W_{\mu, \mu_c} : \text{SO}(3) \times \text{GL}^+(3) \rightarrow \mathbb{R}_0^+$,

$$W_{\mu, \mu_c}(R; F) := \mu \|\text{sym}(R^T F - \mathbb{1})\|^2 + \mu_c \|\text{skew}(R^T F - \mathbb{1})\|^2. \quad (1.1)$$

The arguments are the deformation gradient field $F := \nabla\varphi : \Omega \rightarrow \text{GL}^+(3)$ induced by a deformation mapping $\varphi : \Omega \rightarrow \Omega_{\text{def}} := \varphi(\Omega)$ and the microrotation field $R : \Omega \rightarrow \text{SO}(3)$ evaluated at a given point of the domain Ω . Further, we use the notation $\text{sym}(X) := \frac{1}{2}(X + X^T)$, $\text{skew}(X) := \frac{1}{2}(X - X^T)$, $\langle X, Y \rangle := \text{tr}[X^T Y]$ and we denote the induced Frobenius matrix norm by $\|X\|^2 := \langle X, X \rangle = \sum_{1 \leq i, j \leq n} X_{ij}^2$. The weight $\mu > 0$ coincides with the Lamé shear modulus from linear elasticity and the weight $\mu_c \geq 0$ can be identified with the so-called Cosserat couple modulus.

The energetic contribution (1.1) arises in any geometrically nonlinear, isotropic and quadratic Cosserat micropolar continuum model. Note that the local energy contribution in a Cosserat model can *always* be expressed as $W = W(\bar{U})$, i.e., as a function of the first Cosserat deformation tensor $\bar{U} := R^T F$. This structure is implied by objectivity requirements and was for the first time observed by the Cosserat brothers [6, p. 123, eq. (43)], see also [10] and [24]. Since \bar{U} is a non-symmetric quantity, the most general isotropic and quadratic expression for the local energy contribution which vanishes identically at the reference state is of the form¹

$$\underbrace{\mu \|\text{sym}(\bar{U} - \mathbb{1})\|^2 + \mu_c \|\text{skew}(\bar{U} - \mathbb{1})\|^2}_{\text{“shear–stretch energy”}} + \underbrace{\frac{\lambda}{2} \text{tr}[\bar{U} - \mathbb{1}]^2}_{\text{“linearized volumetric energy”}}. \quad (1.2)$$

¹Note that the Cosserat brothers never proposed any specific expression for the local energy $W = W(\bar{U})$, i.e., they never proposed a constitutive material model inside their original Cosserat framework, as Eringen correctly observes in the introduction of [10]. Linear Cosserat theory was developed only some 50 years later. The particular quadratic ansatz for $W = W(\bar{U})$ considered here, is motivated by a direct extension of the quadratic energy in the linear theory of Cosserat models, see, e.g. [16, 34, 35]. A physical motivation for (1.1) with $\mu_c = 0$ will be given in Section 2.

The parameter λ can be identified with the second Lamé parameter. In the following, we dispense with the corresponding term, since it couples the rotational and volumetric response; a feature not present in the isotropic, geometrically linear Cosserat model.

In [12], we have proved a still surprising reduction lemma [12, Lem. 2.2, p. 4] for the material parameters (weights) μ and μ_c which is valid for *all* space dimensions $n \geq 2$. This lemma singles out a *classical parameter range* $\mu_c \geq \mu > 0$ and a *non-classical parameter range* $\mu > \mu_c \geq 0$ for μ and μ_c and reduces both ranges to an associated limit case. The *classical limit case* is given by $(\mu, \mu_c) = (1, 1)$ and the *non-classical limit case* is given by $(\mu, \mu_c) = (1, 0)$. Exploiting the parameter reduction [12, Lem. 2.2, p. 4] for Problem 1.1 below, we were able to discuss and classify the solutions in dimension $n = 2$. Thus a crucial observation was made: the classical and the non-classical parameter ranges for μ and μ_c characterize a classical and a non-classical regime for the optimal Cosserat rotations. Most importantly, the latter allows for interesting new rotation patterns.

Subsequently, in [13], we have applied computer algebra to the challenging three-dimensional

Problem 1.1 (Weighted optimality in dimension $n = 3$). *Let $\mu > 0$ and $\mu_c \geq 0$. Compute the set of optimal rotations*

$$\arg \min_{R \in \text{SO}(3)} W_{\mu, \mu_c}(R; F) := \arg \min_{R \in \text{SO}(3)} \left\{ \mu \|\text{sym}(R^T F - \mathbb{1})\|^2 + \mu_c \|\text{skew}(R^T F - \mathbb{1})\|^2 \right\} \quad (1.3)$$

for given parameter $F \in \text{GL}^+(3)$ with distinct singular values $\sigma_1 > \sigma_2 > \sigma_3 > 0$.

The resulting explicit expressions allowed us to extract a non-classical geometric mechanism represented by the non-classical minimizers. It is the principal goal of the current paper to study this *relaxed-polar* mechanism in an interesting scenario.

In what follows $\text{polar}(F) \in \text{SO}(3)$ denotes the unique orthogonal factor of the right polar decomposition $F = \text{polar}(F)U(F)$, where $F := \nabla\varphi \in \text{GL}^+(3)$ is the deformation gradient. The right Biot-stretch tensor $U(F) := \sqrt{F^T F} \in \text{Sym}^+(3)$ is positive definite symmetric. Furthermore, we make the assumption that the singular values of $F \in \text{GL}^+(3)$ satisfy $\sigma_1 > \sigma_2 > \sigma_3 > 0$. Recall that the singular values of $F \in \text{GL}^+(3)$ are defined as the eigenvalues of $U = \sqrt{F^T F} \in \text{Sym}^+(3)$.

As suggested by the nomenclature, the polar factor $\text{polar}(F)$ is the *unique* minimizer for (1.1) in the *classical* parameter range $\mu_c \geq \mu > 0$, for all $n \geq 2$. For this generalized version of Grioli's theorem, see [14, 23, 36], or [12, Cor. 2.4, p. 5]. This variational characterization of the polar factor inspired us to introduce the following

Definition 1.2 (Relaxed polar factor(s)). *Let $\mu > 0$ and $\mu_c \geq 0$. We denote the set-valued mapping that assigns to a given parameter $F \in \text{GL}^+(3)$ its associated set of energy-minimizing rotations by*

$$\text{rpolar}_{\mu, \mu_c}(F) := \arg \min_{R \in \text{SO}(3)} W_{\mu, \mu_c}(R; F).$$

By now, the classical parameter domain $\mu_c \geq \mu > 0$ is very well understood. This allows us to focus entirely on the non-classical parameter range $\mu > \mu_c \geq 0$ in our efforts to solve Problem 1.1. Furthermore, the parameter reduction lemma [12, Lem. 2.2, p. 4] states that it is sufficient to solve the non-classical limit case $(\mu, \mu_c) = (1, 0)$, since it implies the following equivalence for all $n \geq 2$:

$$\arg \min_{R \in \text{SO}(3)} W_{\mu, \mu_c}(R; F) = \arg \min_{R \in \text{SO}(3)} W_{1,0}(R; \tilde{F}_{\mu, \mu_c}). \quad (1.4)$$

On the right hand side, we notice a *rescaled deformation gradient*

$$\tilde{F}_{\mu, \mu_c} := \lambda_{\mu, \mu_c}^{-1} F \in \text{GL}^+(3)$$

which is obtained from $F \in \text{GL}^+(3)$ by multiplication with the inverse of the *induced scaling parameter* $\lambda_{\mu, \mu_c} := \frac{\mu}{\mu - \mu_c} > 0$. We note that we use the previous notation throughout the text and further introduce the *singular radius* $\rho_{\mu, \mu_c} := \frac{2\mu}{\mu - \mu_c}$.

It follows that the set of optimal Cosserat rotations can be described by

$$\text{rpolar}_{\mu, \mu_c}(F) = \text{rpolar}_{1,0}(\tilde{F}_{\mu, \mu_c}) \quad (1.5)$$

for the entire non-classical parameter range $\mu > \mu_c \geq 0$. Based on our derivation presented in Section 2, it is for the most part sufficient to focus our discussion on the distinguished non-classical limit case $\mu_c = 0$. As it turns out, there are at most two non-classical minimizing branches of rotations $\text{rpolar}_{\mu, \mu_c}^{\pm}(F)$ in the non-classical parameter range which we can distinguish by a sign; see (1.16) for the definition. Note that for every shear modulus $\mu > 0$ and fixed choice of sign, we have

$$\text{rpolar}_{\mu, 0}^{\pm}(F) = \text{rpolar}_{1, 0}^{\pm}(F). \quad (1.6)$$

1.1 The locally energy-minimizing Cosserat rotations $\text{rpolar}_{\mu, \mu_c}^{\pm}(F)$

We briefly present the geometric characterization of the optimal Cosserat rotations $\text{rpolar}_{\mu, \mu_c}^{\pm}(F)$ obtained in [13]. Let $R \in \text{SO}(n)$ for $n = 2, 3$ and let $\mathbb{S}^2 \subset \mathbb{R}^3$ denote the unit 2-sphere. In dimension $n = 3$, we use the well-known angle-axis parametrization of rotations which we write as $[\alpha, r]$ and which allows to parametrize $R \in \text{SO}(3)$.² Here the rotation angle is $\alpha \in (-\pi, \pi]$ and $r \in \mathbb{S}^2$ specifies the oriented rotation axis.

In order to reduce the parameter space $\text{GL}^+(3)$, we use the (unique) polar decomposition³ $F = \text{polar}(F)U$ and the (non-unique) spectral decomposition of $U = \sqrt{F^T F} \in \text{Sym}^+(3)$ given by $U = QDQ^T$, $Q \in \text{SO}(3)$, and expand

$$R^T F = R^T \text{polar}(F)U = R^T \text{polar}(F)QDQ^T. \quad (1.7)$$

Here, the diagonal matrix $D = \text{diag}(\sigma_1, \sigma_2, \sigma_3)$ contains the eigenvalues of U on its diagonal. These are, by definition, the singular values of $F \in \text{GL}^+(3)$. Note that this is a particular form of the singular value decomposition (SVD). If, furthermore, F has only simple singular values, then it is always possible to choose the rotation $Q \in \text{SO}(3)$ such that an ordering $\sigma_1 > \sigma_2 > \sigma_3 > 0$ is achieved.

Exploiting that $Q \in \text{SO}(3)$, we now transform the Cosserat shear–stretch energy into principal axis coordinates. This simplification makes use of the isotropy of the energy. For the actual computation, note first that

$$\begin{aligned} Q^T (\text{sym}(R^T F) - \mathbb{1})Q &= Q^T (\text{sym}(R^T \text{polar}(F)QDQ^T) - \mathbb{1})Q \\ &= \text{sym}(Q^T R^T \text{polar}(F)QDQ^T Q - Q^T Q) = \text{sym}(\underbrace{Q^T R^T \text{polar}(F)Q}_=: \widehat{R} D - \mathbb{1}) = \text{sym}(\widehat{R} D - \mathbb{1}). \end{aligned} \quad (1.8)$$

In the process, it is natural to introduce a *relative* rotation

$$\widehat{R} := Q^T R^T \text{polar}(F)Q \quad (1.9)$$

which acts relative to the continuum rotation $\text{polar}(F)$. The action of \widehat{R} is defined with respect to the coordinate system induced by the columns of Q , i.e., in a positively oriented frame of principal directions of U . This interpretation is also underlined by the inverse formula

$$R = \left(Q \widehat{R} Q^T \text{polar}(F)^T \right)^T = \text{polar}(F) Q \widehat{R}^T Q^T. \quad (1.10)$$

The last relation allows us to recover the original absolute rotation R from the relative rotation \widehat{R} . Our next step is to insert the transformed symmetric part (1.8) into the definition of

$$W_{1,0}(R; F) = \|\text{sym}(R^T F - \mathbb{1})\|^2 = \|Q^T \text{sym}(R^T F - \mathbb{1})Q\|^2 = \|\text{sym}(\widehat{R} D - \mathbb{1})\|^2, \quad (1.11)$$

where we have used that the conjugation by Q^T preserves the Frobenius matrix norm. Along the same lines, we can reduce the shear-stretch energy for general $\mu > 0$ and $\mu_c \geq 0$, as is easy to see. It follows, that it is sufficient to solve for the relative rotation, i.e., we may consider

²The angle-axis parametrization is singular, but this is not an issue for our exposition.

³For an introduction to the polar and singular value decomposition, see, e.g., [46] and for recent related results on fundamental variational characterizations of the polar factor $\text{polar}(F)$, see [19, 36, 39] and references therein.

Problem 1.3 (Diagonal form of weighted optimality in $n = 3$). *Let $\mu > 0$ and $\mu_c \geq 0$ and let $D = \text{diag}(\sigma_1, \sigma_2, \sigma_3)$ with $\sigma_1 > \sigma_2 > \sigma_3 > 0$. Compute the set of optimal relative rotations*

$$\arg \min_{\widehat{R} \in \text{SO}(3)} W_{\mu, \mu_c}(\widehat{R}^T; D) := \arg \min_{\widehat{R} \in \text{SO}(3)} \left\{ \mu \left\| \text{sym}(\widehat{R}D - \mathbb{1}) \right\|^2 + \mu_c \left\| \text{skew}(\widehat{R}D - \mathbb{1}) \right\|^2 \right\} \quad (1.12)$$

for a given diagonal matrix D .

We stress that the rotation angle of the relative rotation \widehat{R} is implicitly reversed due to the correspondence $R^T \leftrightarrow \widehat{R}$.

The computation of the solutions to Problem 1.3 by computer algebra together with a statistical verification is one of the core results obtained in [13] which we present next.

Proposition 1.4 (Energy-minimizing relative rotations for $(\mu, \mu_c) = (1, 0)$). *Let $\sigma_1 > \sigma_2 > \sigma_3 > 0$ be the singular values of $F \in \text{GL}^+(3)$. Then the energy-minimizing relative rotations solving Problem 1.3 are given by*

$$\widehat{R}_{1,0}^\pm(F) := \begin{pmatrix} \cos \hat{\beta}_{1,0}^\pm & -\sin \hat{\beta}_{1,0}^\pm & 0 \\ \sin \hat{\beta}_{1,0}^\pm & \cos \hat{\beta}_{1,0}^\pm & 0 \\ 0 & 0 & 1 \end{pmatrix}, \quad (1.13)$$

where the optimal rotation angles $\hat{\beta}_{1,0}^\pm \in (-\pi, \pi]$ are given by

$$\hat{\beta}_{1,0}^\pm(F) := \begin{cases} 0 & , \text{ if } \sigma_1 + \sigma_2 \leq 2, \\ \pm \arccos\left(\frac{2}{\sigma_1 + \sigma_2}\right) & , \text{ if } \sigma_1 + \sigma_2 \geq 2. \end{cases} \quad (1.14)$$

Thus, in the non-classical regime $\sigma_1 + \sigma_2 \geq 2$, we obtain the explicit expression

$$\widehat{R}_{1,0}^\pm(F) := \begin{pmatrix} \frac{2}{\sigma_1 + \sigma_2} & \mp \sqrt{1 - \left(\frac{2}{\sigma_1 + \sigma_2}\right)^2} & 0 \\ \pm \sqrt{1 - \left(\frac{2}{\sigma_1 + \sigma_2}\right)^2} & \frac{2}{\sigma_1 + \sigma_2} & 0 \\ 0 & 0 & 1 \end{pmatrix}. \quad (1.15)$$

In the classical regime $\sigma_1 + \sigma_2 \leq 2$, we simply obtain the relative rotation $\widehat{R}_{1,0}^\pm(F) = \mathbb{1}$, and there is no deviation from the polar factor $\text{polar}(F)$ at all.

The corresponding *absolute* representation of the optimal Cosserat rotations is uniquely determined by the relation (1.10), which leads us to define

$$\text{rpolar}_{1,0}^\pm(F) := \text{polar}(F) Q(F) \left(\widehat{R}_{1,0}^\pm(F) \right)^T Q(F)^T. \quad (1.16)$$

Furthermore, due to the parameter reduction [12, Lem. 2.2], it is always possible to recover the optimal rotations $\text{rpolar}_{\mu, \mu_c}^\pm(F)$ for general non-classical parameter choices $\mu > \mu_c \geq 0$ from the non-classical limit case $(\mu, \mu_c) = (1, 0)$; cf. [12] and [13] for details. For now, we shall defer the explicit procedure, since it is quite instructive to interpret the distinguished non-classical limit case $\mu = 1$ and $\mu_c = 0$ first.

1.2 Geometric-mechanical aspects of optimal Cosserat rotations

It seems natural to introduce

Definition 1.5 (Maximal mean planar stretch and strain). *Let $F \in \text{GL}^+(3)$ with singular values $\sigma_1 \geq \sigma_2 \geq \sigma_3 > 0$. We introduce the **maximal mean planar stretch** u^{mmp} and the **maximal mean planar strain** s^{mmp} as follows:*

$$\begin{aligned} u^{\text{mmp}}(F) &:= \frac{\sigma_1 + \sigma_2}{2}, \quad \text{and} \\ s^{\text{mmp}}(F) &:= \frac{(\sigma_1 - 1) + (\sigma_2 - 1)}{2} = u^{\text{mmp}}(F) - 1. \end{aligned} \quad (1.17)$$

In order to describe the bifurcation behavior of $\text{rpolar}_{\mu, \mu_c}^{\pm}(F)$ as a function of the parameter $F \in \text{GL}^+(3)$, it is helpful to partition the parameter space $\text{GL}^+(3)$.

Definition 1.6 (Classical and non-classical domain). *To any pair of material parameters (μ, μ_c) in the non-classical range $\mu > \mu_c \geq 0$, we associate a **classical domain** D_{μ, μ_c}^C and a **non-classical domain** $D_{\mu, \mu_c}^{\text{NC}}$. Here,*

$$\begin{aligned} D_{\mu, \mu_c}^C &:= \{F \in \text{GL}^+(3) \mid s^{\text{mmp}}(\tilde{F}_{\mu, \mu_c}) \leq 0\}, \quad \text{and} \\ D_{\mu, \mu_c}^{\text{NC}} &:= \{F \in \text{GL}^+(3) \mid s^{\text{mmp}}(\tilde{F}_{\mu, \mu_c}) \geq 0\}, \end{aligned} \quad (1.18)$$

respectively.

It is straight-forward to derive the following equivalent characterizations

$$\begin{aligned} D_{\mu, \mu_c}^C &= \{F \in \text{GL}^+(3) \mid u^{\text{mmp}}(F) \leq \lambda_{\mu, \mu_c}\} = \{F \in \text{GL}^+(3) \mid \sigma_1 + \sigma_2 \leq \rho_{\mu, \mu_c} := \frac{2\mu}{\mu - \mu_c}\}, \\ D_{\mu, \mu_c}^{\text{NC}} &= \{F \in \text{GL}^+(3) \mid u^{\text{mmp}}(F) \geq \lambda_{\mu, \mu_c}\} = \{F \in \text{GL}^+(3) \mid \sigma_1 + \sigma_2 \geq \rho_{\mu, \mu_c} := \frac{2\mu}{\mu - \mu_c}\}. \end{aligned} \quad (1.19)$$

On the intersection $D_{\mu, \mu_c}^C \cap D_{\mu, \mu_c}^{\text{NC}} = \{F \in \text{GL}^+(3) \mid s^{\text{mmp}}(F) = 0\}$, the minimizers $\text{rpolar}_{\mu, \mu_c}^{\pm}(F)$ coincide with the polar factor $\text{polar}(F)$. This can be seen from the form of the optimal relative rotations in Proposition 1.4. More explicitly, in dimension $n = 3$ and in the non-classical limit case $(\mu, \mu_c) = (1, 0)$, we have:

$$D_{1,0}^C := \{F \in \text{GL}^+(3) \mid s^{\text{mmp}}(F) \leq 0\}, \quad \text{and} \quad D_{1,0}^{\text{NC}} := \{F \in \text{GL}^+(3) \mid s^{\text{mmp}}(F) \geq 0\}. \quad (1.20)$$

Since the maximal mean planar strain $s^{\text{mmp}}(F)$ is related to strain, this indicates a particular (possibly new) type of tension-compression asymmetry.

Towards a geometric interpretation of the energy-minimizing Cosserat rotations $\text{rpolar}_{1,0}^{\pm}(F)$ in the non-classical limit case $(\mu, \mu_c) = (1, 0)$, we reconsider the spectral decomposition of $U = QDQ^T$ from the principal axis transformation in Section 1. Let us denote the columns of $Q \in \text{SO}(3)$ by $q_i \in \mathbb{S}^2$, $i = 1, 2, 3$. Then q_1 and q_2 are orthonormal eigenvectors of U which correspond to the largest two singular values σ_1 and σ_2 of $F \in \text{GL}^+(3)$. More generally, we introduce the following concept

Definition 1.7 (Plane of maximal stretch). *The **plane of maximal stretch** is the linear subspace*

$$P^{\text{ms}}(F) := \text{span}(\{q_1, q_2\}) \subset T_x \Omega$$

spanned by the two maximal eigenvectors q_1, q_2 of U , i.e., the eigenvectors associated to the two largest singular values $\sigma_1 > \sigma_2 > \sigma_3 > 0$ of the deformation gradient $F \in \text{GL}^+(3)$.

In an analogous fashion, we obtain the plane of maximal stretch in the deformed configuration as

$$P_{\text{def}}^{\text{ms}}(F) := \text{polar}(F) P^{\text{ms}}(F) \subset T_{\varphi(x)} \Omega_{\text{def}}. \quad (1.21)$$

Previously, in our Proposition 1.4, we have determined the energy-minimizing relative rotations

$$\widehat{R}_{1,0}^{\pm}(D) := \arg \min_{\widehat{R} \in \text{SO}(3)} \widehat{W}_{1,0}(\widehat{R}, D) := \arg \min_{\widehat{R} \in \text{SO}(3)} \left\| \text{sym}(\widehat{R}D) - \mathbf{1} \right\|^2.$$

Before we proceed, it seems worthwhile to repeat that for $u^{\text{mmp}}(F) \leq 1$, we have $F \in D_{1,0}^C$ and we have $\widehat{R}_{1,0}^{\pm}(D) = \mathbf{1}$. Here, the identity matrix considered as a relative rotation corresponds to the polar factor $\text{polar}(F)$ as an absolute rotation. In strong contrast, the minimizers $\text{rpolar}_{1,0}^{\pm}(F)$ deviate strictly from $\text{polar}(F)$ for $u^{\text{mmp}}(F) > 1$ which implies $F \in D_{1,0}^{\text{NC}} \setminus D_{1,0}^C$. Only in this latter case the relaxed-polar mechanism induces non-classical rotation patterns.

Let us now look at the interesting non-classical case $F \in D_{1,0}^{\text{NC}}$ in some more detail.

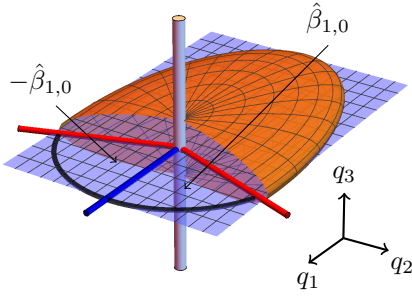


Figure 1.1: Action of $\text{rpol}_{1,0}^{\pm}(F)$ in axes of principal stretch for a stretch ellipsoid with half-axes $(\nu_1, \nu_2, \nu_3) = (4, 2, 1/2)$. The plane of maximal stretch $\text{P}^{\text{ms}}(F)$ is depicted in blue. The cylinder along $q_3 \perp \text{P}^{\text{ms}}(F)$ illustrates that the axis of rotation is the eigenvector q_3 of U associated with the smallest singular value $\nu_3 = 1/2$ of F . The thin cylinder [blue] bisecting the opening represents the relative rotation angle $\hat{\beta} = 0$ and corresponds to $\text{polar}(F)$. The outer two cylinders [red] correspond to the two non-classical minimizers $\text{rpol}_{1,0}^{\pm}(F)$. The enclosed angles $\hat{\beta}_{1,0}^{\pm} = \pm \arccos(\frac{2}{\nu_1 + \nu_2})$ are the optimal relative rotation angles. This reveals the major symmetry of the non-classical minimizers.

Remark 1.8 ($\text{rpol}_{1,0}^{\pm}(F)$ in the non-classical domain). *If $F \in \text{D}_{1,0}^{\text{NC}}$, then by definition $s^{\text{mmp}}(F) > 0$ and the maximal mean planar strain is expansive. The deviation of the non-classical energy-minimizing rotations $\text{rpol}_{1,0}^{\pm}(F)$ from the polar factor $\text{polar}(F)$ is measured by a rotation in the plane of maximal stretch $\text{P}^{\text{ms}}(F)$ given by $\text{polar}(F)^T \text{rpol}_{1,0}^{\pm}(F) = Q(F) \widehat{R}_{1,0}^{\mp}(F) Q(F)^T$. The rotation axis is the eigenvector q_3 associated with the smallest singular value $\sigma_3 > 0$ of the deformation gradient $F := \nabla \varphi$ and the relative rotation angle is given by $\hat{\beta}_{1,0}^{\mp}(F) = \mp \arccos\left(\frac{1}{u^{\text{mmp}}(F)}\right)$.*

The absolute value of the rotation angle $|\hat{\beta}_{1,0}^{\pm}(F)|$ increases monotonically and we have the asymptotic limits

$$\lim_{u^{\text{mmp}}(F) \rightarrow \infty} \hat{\beta}_{1,0}^{\pm}(F) = \pm \frac{\pi}{2}.$$

In angle-axis representation, we obtain

$$\begin{aligned} \widehat{R}_{1,0}^{\pm}(F) &\equiv \left[\pm \arccos\left(\frac{1}{u^{\text{mmp}}(F)}\right), (0, 0, 1) \right], \quad \text{and} \\ \text{polar}(F)^T \text{rpol}_{1,0}^{\pm}(F) &\equiv \left[\mp \arccos\left(\frac{1}{u^{\text{mmp}}(F)}\right), q_3 \right]. \end{aligned} \quad (1.22)$$

In the last equation, we have used that $\text{rpol}_{1,0}^{\pm}(F) = \text{polar}(F) Q \widehat{R}_{1,0}^{\mp} Q^T$. Note the flip of signs in the definition of the optimal branches $\text{rpol}_{1,0}^{\pm}(F)$ arising from the definition in terms of the optimal relative rotations $(\widehat{R}_{1,0}^{\pm})^T = \widehat{R}_{1,0}^{\mp}$.

This paper is now structured as follows: in Section 2 we work out a connection between the variational formulation of a full Cosserat model, the variationally optimal Cosserat rotations $\text{rpol}_{\mu,0}^{\pm}(F)$, and plasticity theory. To this end, a sequence of assumptions is made. Essentially, we assume that the plastic distortion is small and rely on a best approximation in the space of symmetric positive definite matrices due to Higham [15] (see Appendix A). In Section 3, we present a synthetic nanoindentation experiment in order to illustrate the non-classical effects realized by the relaxed polar mechanism $\text{rpol}_{1,0}^{\pm}(F)$. Nanoindentation is a setting of considerable interest, because non-classical rotation patterns can be experimentally observed, see, e.g., [53]. Our development in Section 2 seems well-adapted to the setting of a nanoindentation experiment. The rotation patterns are then compared to experiments due to Zafarani et al. [8, 51–53]. We conclude this paper with a short summary in Section 4. Finally, we briefly present Higham's best approximation in the space of symmetric positive definite matrices [15] and the algorithmic implementation of $\text{rpol}_{1,0}^{\pm}(F)$ in the Appendix.

2 Multiplicative plasticity, small elastic distortions and Cosserat theory

Our intention is to illustrate the non-classical *relaxed-polar* mechanism discovered in [12] and [13]. Note that this is just one particular aspect of a broad series of investigations on generalized plasticity and microstructure by the second author; see, e.g., [28–30] and [26] for extensive preliminary work by the second author.

More precisely, we describe the energy-optimal rotation mechanism realized by the two rotations $\text{rpolar}_{\mu, \mu_c}^{\pm}(F)$, and patterns that might arise by combinations thereof. It is natural to expect combinations of the two patterns to arise in the full model, since the Cosserat model has the structure of a diffuse interface equation for the field of microrotations. We present this new rotational mechanism in the setting of nanoindentation experiments where non-classical rotation patterns can be observed.⁴ To this end, we carry out a comparison of the induced rotation patterns in an idealized nanoindentation⁵ with experimentally obtained measurements from nanoindentation into copper single crystals. This comparison is the subject of Section 3.

2.1 The strain energy density in isotropic multiplicative plasticity for negligible elastic strains

Before we proceed to the beforementioned comparison in the next section, we want to work out a *possible* connection between the plasticity in the deformation of crystalline metals through a series of modelling assumptions and subsequent simplifications. Based on this development, we show that it is possible to recover the minimization problem with zero Cosserat couple modulus, i.e., with $\mu_c = 0$. This leads to the optimal Cosserat rotations $\text{rpolar}_{\mu, 0}^{\pm}(F)$ which are locally energy-optimal rotations, i.e., at every point in the domain Ω . Note that this establishes a link between the local minimization of the shear-stretch energy with respect to rotations, i.e., our Problem 1.1, and the framework of finite multiplicative plasticity theory for small internal length scales $L_c \ll 1$.

In what follows, we consider the setting of a nanoindentation experiment after the removal of the indenter and the subsequent elastic relaxation of the indented specimen.

The starting point of our development is the (by now) well-known multiplicative decomposition

$$F = F_e F_p, \quad \text{with } (F_e, F_p) \in \text{GL}^+(3) \times \text{SL}(3), \quad (2.1)$$

of the (macroscopic) deformation gradient $F := \nabla\varphi$; a succinct historic account is given in [45]. Note that the elastic part $F_e \in \text{GL}^+(3)$ and the plastic part $F_p \in \text{SL}(3)$ are in general incompatible (non-integrable): the elastic and plastic two-point tensor fields F_e and F_p do, in general, *not* arise as the derivative of a suitably chosen global deformation mapping, in strong contrast to the deformation gradient field $F = \nabla\varphi$, which they factor.

We shall make use of the following left and right polar decompositions

$$F_e = R_e U_e = V_e R_e, \quad \text{and } F_p = R_p U_p. \quad (2.2)$$

By $R_e \in \text{SO}(3)$ we denote the orthogonal factor of the polar decomposition of the elastic part (elastic rotation) and by $R_p \in \text{SO}(3)$ the orthogonal factor of the polar decomposition of the plastic part (plastic rotation). Furthermore, $V_e := \sqrt{F_e F_e^T}$, $U_e := \sqrt{F_e^T F_e} \in \text{Sym}^+(3)$ are the left and right elastic stretch tensors, respectively, and $U_p := \sqrt{F_p^T F_p} \in \text{Sym}^+(3)$ denotes the right plastic stretch tensor. Applying now the polar decomposition to the multiplicative split (2.1), we obtain

$$F = F_e F_p = V_e R_e R_p U_p = V_e R U_p, \quad \text{where } R := R_e R_p. \quad (2.3)$$

In what follows, we shall refer to the combined rotation $R := R_e R_p$ as the *microrotation* induced by F . We shall also find the related expansion

$$F = F_e F_p = R_e U_e R_p U_p \quad (2.4)$$

⁴Following our nomenclature introduced in [12] and [13], the term non-classical refers to rotation patterns which deviate from the macroscopic field of continuum rotations $\text{polar}(F)$.

⁵By “synthetic” and “idealized”, we indicate that we do not consider (numerical) solutions of a realistic Cosserat boundary value problem. Towards a better understanding of the relaxed-polar mechanism it seems more instructive to start with the simpler case of a prescribed deformation mapping.

to be useful.

Elastoplasticity combines two fundamentally different mechanical mechanisms. Likewise, the mechanical energy expended in plastically deforming a solid can be partitioned into recoverable elastic work and plastic work. The plastic work dissipates to a large part in the form of heat. What remains of it, stored in the solid, is referred to as the *stored energy of cold work*. In crystalline solids this energy is stored in an evolving defect structure which is primarily characterized by lattice dislocations [40, 41, 48, 49]; cf. also [1]. We refer to the associated mechanical processes in the material as strain hardening.

Returning to our setting of nanoindentation into copper single crystals, we *postulate* (as is often done) that the orthogonal factor of the elastic part $R_e(F_e) \in \text{SO}(3)$ corresponds to rotations of the atomic lattice. It is important to realize that the microstructure need not conform to the macroscopic deformation which can be experimentally observed. Hence, it is reasonable to model lattice rotations by a suitable independent degree of freedom, e.g., a microrotation field R . Note further that the elastic rotations $R_e \in \text{SO}(3)$ are usually assumed to be reversible, see, e.g., [25, 37], whereas the orthogonal factor of the plastic part $R_p(F_p) \in \text{SO}(3)$ is usually assumed to correspond to irreversible plastic rotations. We further make the assumption that the stored energy content of a copper specimen can be well described by three contributions

$$W_{\text{total}} = \underbrace{W_{\text{elastic}}(U_e)}_{\text{elastically recoverable}} + \underbrace{W_{\text{hardening}}(U_p)}_{\text{linear kin. hardening}} + \underbrace{W_{\text{defect}}(R, F_p)}_{\text{incompatibility measure}} . \quad (2.5)$$

total energy of cold work

This hypothesis is in general agreed on for the case of metallic materials. Since we imagine the possibility to describe essential effects of the deformation in an isotropic setting, we consider an isotropic elastic energy of the type

$$W_{\text{elastic}}(U_e) = \mu_e \|\text{dev log } U_e\|^2 + \frac{\kappa_e}{2} \text{tr} [\log U_e]^2 , \quad (2.6)$$

which is geometrically nonlinear, but physically linear in $\log(U_e)$. Here μ_e and κ_e are the isotropic Lamé shear modulus and the isotropic bulk modulus of linear elasticity. Energies of this type have recently been investigated in [31, 32] where they have been finally given a natural differential geometric interpretation. Similarly, we consider for the first contribution of the energy of cold work

$$W_{\text{hardening}}(U_p) = \mu_{\text{micro}} \|\text{dev log } U_p\|^2 + \frac{\kappa_{\text{micro}}}{2} \text{tr} [\log U_p]^2 . \quad (2.7)$$

Here μ_{micro} is the isotropic shear hardening modulus and κ_{micro} is the isotropic bulk hardening modulus.

It suffices to consider the physics of the indentation process after the unloading procedure of the indenter was completed and the subsequent elastic relaxation has converged to an equilibrium state. It is then natural to presume that the elastic strains which still remain in the specimen are very small. Thus, we consider the so-called regime of nearly rigid plasticity which amounts to

$$\|U_e - \mathbf{1}\| = \|V_e - \mathbf{1}\| \ll 1 \quad (2.8)$$

and $F_p \in \text{SL}(3)$, i.e., plastic incompressibility. The latter is a standard assumption in finite plasticity and we have already made it early on. Based on our assumption that the remaining residual elastic strains in the specimen are negligible after elastic relaxation, we discard the elastic energy contribution altogether and are left only with the strain hardening and dislocation-related defect contributions. Due to $F_p \in \text{SL}(3)$, the strain hardening energy simplifies to

$$W_{\text{hardening}}(U_p) = \mu_{\text{micro}} \|\log U_p\|^2 . \quad (2.9)$$

For small plastic strains $\|U_p - \mathbf{1}\| \ll 1$, (2.9) is certainly well-approximated by the quadratic energy

$$W_{\text{hardening}}(U_p) = \mu_{\text{micro}} \|U_p - \mathbf{1}\|^2 , \quad (2.10)$$

which does admit an interpretation as a measure for accumulated plastic slip.

2.2 Symmetric best-approximation of the plastic stretch and complete spatial decoupling

It turns out that the assumption of small elastic strains (2.8) leads us to the following interesting approximation of the plastic stretch U_p . We start with the expansion of the deformation gradient

$$F = V_e R_e R_p U_p \approx \mathbb{1} R_e R_p U_p = R U_p \quad (2.11)$$

and subsequently solve for the plastic stretch which yields

$$U_p \approx \widetilde{U}_p := R^T F = (R_e R_p)^T F. \quad (2.12)$$

This seems fine on first glance, however, the usual geometric interpretation of the plastic stretch tensor requires $U_p \in \text{Sym}^+(3)$ which is violated by \widetilde{U}_p . On these grounds a positive definite symmetric approximation is certainly desirable. An intuitive solution is to compute a best approximation (relative to the Frobenius matrix norm) of \widetilde{U}_p in the closed cone of positive-semidefinite matrices which we denote by $\overline{\text{Sym}^+(3)}$. A theorem due to Higham (see [15], provided in our Appendix A) allows to precisely characterize the unique best approximation and we shall denote it by $\pi(\widetilde{U}_p)$. The following characterization is then intuitive: the best-approximation $\pi(\widetilde{U}_p)$ is the projection onto the symmetric part, i.e.,

$$U_p \approx \pi(\widetilde{U}_p) = \text{sym}(\widetilde{U}_p) = \text{sym}(R^T F) = \text{sym}((R_e R_p)^T F). \quad (2.13)$$

This simple characterization is valid as long as $\|F - R_e R_p\| < 1$, see Appendix A. Furthermore, the defect in symmetric positive-definiteness of \widetilde{U}_p is necessarily small due to our assumption $V_e \approx \mathbb{1}$.

In what follows, we introduce the contribution⁶ W_{defect} in terms of the square norm of a version of the Burgers' tensor appropriate for the Cosserat setting we employ. Since such a choice involves the derivative of F_p , we are clearly in a gradient-plasticity context (cf. also [30] and [29]). More precisely, we model the dislocation-related defect energy contribution by

$$W_{\text{defect}}(R_e, F_p) := \frac{\mu_e L_c^2}{2} \underbrace{\| (R_e F_p)^T \text{Curl}(R_e F_p) \|^2}_{\text{defect density}}. \quad (2.14)$$

This dislocation-related defect-energy measures the joint incompatibility of $R_e F_p$. For an interpretation, note that the term $R_e F_p$ approximates the deformation gradient in the context of our small elastic strain hypothesis $V_e \approx \mathbb{1}$, since

$$\nabla \varphi = F = V_e R_e F_p \approx R_e F_p. \quad (2.15)$$

Thus the proposed incompatibility measure (2.14) penalizes the extent to which $R_e F_p$ is not an integrable tensor field and can be interpreted as an approximation to the well-known dislocation energy density $\frac{\mu_e L_c^2}{2} \|F_p^T \text{Curl} F_p\|^2$.⁷ Therefore, (2.14) fully takes into account the remaining eigenstresses due to incompatibility.

Finally, we combine the approximation of the strain hardening contribution with the previously derived dislocation-related energy measure which yields the remaining total energy of cold work

$$\begin{aligned} W(R_e, F_p) &= \mu_{\text{micro}} \left\| \pi(\widetilde{U}_p) - \mathbb{1} \right\|^2 + \frac{\mu_e L_c^2}{2} \left\| (R_e F_p)^T \text{Curl}(R_e F_p) \right\|^2 \\ &= \mu_{\text{micro}} \left\| \text{sym}((R_e R_p)^T F) - \mathbb{1} \right\|^2 + \frac{\mu_e L_c^2}{2} \left\| (R_e F_p)^T \text{Curl}(R_e F_p) \right\|^2. \end{aligned} \quad (2.16)$$

Inspection of (2.16) in the context of our idealized nanoindentation shows that the energy of cold work corresponds approximatively to the energy stored in the remaining total shape change.

Finally, considering again that $U_p \approx \mathbb{1}$, we can also approximate $F_p \approx R_p$ in the dislocation-related defect-energy and the energy takes the form

$$\begin{aligned} W(R_e, F_p) &= \mu_{\text{micro}} \left\| \text{sym}((R_e R_p)^T F) - \mathbb{1} \right\|^2 + \frac{\mu_e L_c^2}{2} \left\| (R_e R_p)^T \text{Curl}(R_e R_p) \right\|^2 \\ &= \mu_{\text{micro}} \left\| \text{sym}(R^T F) - \mathbb{1} \right\|^2 + \frac{\mu_e L_c^2}{2} \left\| R^T \text{Curl} R \right\|^2. \end{aligned} \quad (2.17)$$

⁶It is reasonable to consider this contribution as a so-called pseudopotential of a dissipative process.

⁷The independent coefficients of $R^T \text{Curl} R$ and $R^T D_x R$ are related by an invertible linear mapping, see [37, p. 153, Eq. (3.9)].

In this simplified setting, we further make the following fundamental⁸

Assumption: (Perfectly localized microstructure) *The microrotations $R = R_e R_p$ adjust themselves so as to instantaneously minimize the (approximated) cold work (2.17) for $L_c = 0$. The microstructure is perfectly decoupled in the variational formulation in the sense that there is no spatial interaction of the microstructure field with itself at all.*

The physical relevance of this assumption is certainly debatable. In fact, we consider it as an intermediate step ourselves, which seems, however, necessary and quite fruitful. A better understanding of the perfectly localized and decoupled limit case $L_c = 0$ seems to lie at the root of a better qualitative understanding of the Cosserat model on small length scales $0 < L_c \ll 1$.

Remark 2.1 (A model without elastic strains by nonlinear projection onto the complementing factors). *Our derived model is heavily based on approximations arising from $U_e \approx \mathbb{1}$ and $V_e \approx \mathbb{1}$. Let us suppose that these assumptions are slightly violated. Then our derived energy is a measure for the leading part of the deformation energy which is generated by elastic rotations and plastic processes only. The replacement of the factors $V_e \mapsto \mathbb{1}$ and $U_e \mapsto \mathbb{1}$ with the identity naturally induces an energetic contribution which is independent of purely elastic strains.⁹ From this point of view, we are simply focussing on the interaction of local rotations R in the specimen with plastic deformation F_p , or plastic strain U_p , equivalently. Essentially, in our development, we suppress the effects due to purely elastic distortions in order to obtain a clear view on the remaining effects.*

Towards the formulation of boundary value problems, we consider the two-field minimization problem

$$\inf_{(\varphi, R)} \int_{\Omega} \mu_{\text{micro}} \|\text{sym}(R^T F - \mathbb{1})\|^2 + \frac{\mu_e L_c^2}{2} \|R^T \text{Curl} R\|^2 \, dV. \quad (2.18)$$

This is the geometrically nonlinear, physically linear Cosserat model with zero Cosserat couple modulus $\mu_c = 0$, see also [27]. In order to gain more insight into the nature of this variational problem, it is certainly a reasonable first step to study the simplified case

$$\inf_{(\varphi, R)} \int_{\Omega} \mu_{\text{micro}} \|\text{sym}(R^T F - \mathbb{1})\|^2 \, dV = \inf_{\varphi} \int_{\Omega} W^{\text{red}}(\nabla \varphi) \, dV, \quad (2.19)$$

where the reduced Cosserat shear-stretch energy is given by

$$W^{\text{red}}(F) := \min_R \mu_{\text{micro}} \|\text{sym}(R^T F - \mathbb{1})\|^2 = \mu_{\text{micro}} \min_R W_{1,0}(R; F). \quad (2.20)$$

At this point, we have finally recovered the minimization problem as stated in Problem 1.1 for the field of microrotations R which we have successfully studied in [12] and [13].

Note that the variational problem (2.18) has been studied previously in the context of simple shear of an infinite block in [38]. There, an infinite strip of height $h = 1$ is fixed at the bottom and sheared at the upper side by an amount $\gamma \in \mathbb{R}$. Solutions of (2.18) are sought for in the restricted class of deformation mappings $\varphi(x_1, x_2, x_3) = (x_1 + u(x_3), x_2, x_3)$ which are of the form of simple glide. Similarly, microrotations $R(x_1, x_2, x_3) = R(x_3)$ with fixed rotation axis e_2 are considered. The boundary conditions for φ are $u(0) = 0$, $u(1) = \gamma$ and for the microrotation field R a consistency condition is imposed. It is then possible to show that uniform simple shear is always critical, however, non-uniform microstructure solutions exist and are energy-optimal. The explicit solutions to the boundary value problem realize a “deck of cards”-mechanism which resembles real deformation patterns also with regard to the phenomenon of counter-rotations, see [9] and Figure 2.1.

2.3 Consistency of the modelling assumptions with the physics of a nanoindentation

It is an important question to which degree the modelling assumptions lead to a valid description of a physical process in a given physical regime. In the nanoindentation experiments carried out by

⁸There is a connection to the notion of a *latent microstructure* (also: latent internal degrees of freedom), which was illuminated in the Discussion of [13].

⁹This can be interpreted as a nonlinear projection onto the remaining factors of the expansion (2.3).

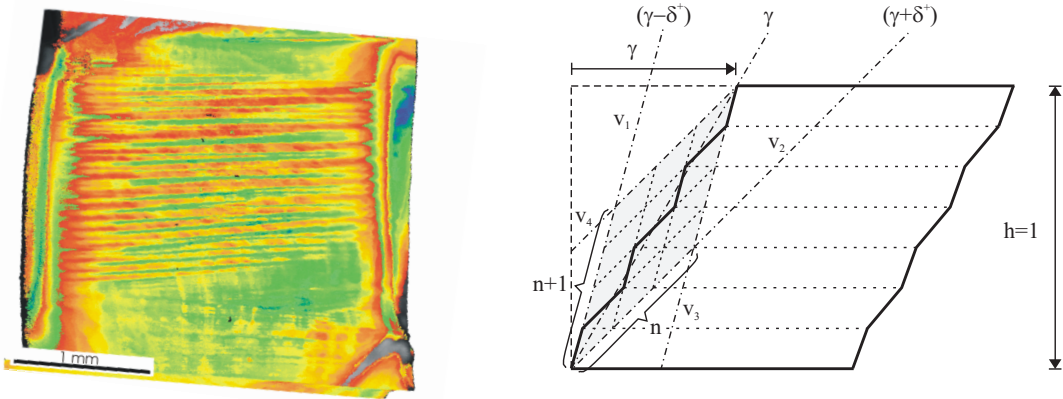


Figure 2.1: *Left*: a single crystal copper specimen in simple shear, revealing glide traces and microbands. Lattice rotations do not coincide with continuum rotations [9] (reproduced with permission). *Right*: macroscopic simple shear as predicted by elastic Cosserat lamination-microstructure solution for $\mu_c = 0$; cf. Problem (2.19). The homogeneous solution is a pointwise limit of the lamination response as the number of laminates tends to infinity. For vanishing characteristic length scale $L_c = 0$ the thickness of the laminates remains indeterminate [38].

Raabe et al. at the Max-Planck Institut für Eisenforschung, Düsseldorf, which we consider here, the total deformation is certainly to a large extent plastic, i.e., $F \approx RF_p$. This requires that RF_p is nearly compatible. (The “synthetic” F presented in the next section is a deformation gradient and hence compatible.) Furthermore, the total deformation is nearly incompressible, since it arises from translation along glide planes. This is a common argument to justify $F_p \in \text{SL}(3)$.

In what follows, we consider experimental results due 3D-EBSD measurements of nanoindentations in solid copper. The experimental method referred here to as 3D-EBSD stands for a tomographic variant of the electron backscatter diffraction technique that allows to reconstruct three-dimensional crystallographic multigrain and multiphase objects by sequential serial sectioning. The full method was described in [17, 18, 54]. Since the measurements in [53] were made after removal of the indenter, the unloaded sample is elastically relaxed but contains remaining local eigenstresses due to incompatibility. Hence, it seems reasonable to expect that $V_e \approx U_e \approx \mathbb{1}$ is valid for the nanoindentation experiments of interest.

On the nanometer length scale, a single crystal copper sample is a highly anisotropic medium. Nonetheless, we may ask the following question: to which degree can the essential deformation modes due to lattice effects, e.g., dislocation glide and lattice rotations, be described by an isotropic model? And which essential features of the macroscopic deformation can be characterized without resorting to the fundamental crystal mechanics? It is mostly accepted that crystal mechanics strongly influence the classical mechanical behavior, i.e., on all scales beyond the realm of quantum physics. However, as the workings realized by anisotropic crystal mechanisms add up on ever coarser scales they are expected to be averaged and homogenized. Thus, the dominating effects on a coarser scale might (or might not) allow for a good approximation by a less anisotropic, or even isotropic, description on a suitably coarse length scale.¹⁰

In his doctoral dissertation [51], Nader Zaafarani, who worked at the Max-Planck Institut für Eisenforschung, Düsseldorf, carried out simulations [51, 53] based on the *physically based crystal plasticity model* with viscoplastic hardening introduced in [21, 22] which produced quite realistic results. Furthermore, in order to demonstrate the failure of a traditional isotropic plasticity model, Zaafarani carried out simulations of nanoindentation processes for an isotropic J_2 -plasticity model. The results clearly reflected the isotropic constitutive model and, as expected, failed to predict the experimentally observed non-classical rotation patterns below a nanoindentation.

Given the complexity of physically based crystal plasticity models and the challenges associated with their mathematical analysis, we pursue the question whether the mathematical framework of isotropic generalized continuum mechanics with additional degrees of freedom, e.g., Cosserat

¹⁰The nanometer length scale of nanomechanics might be too fine as a mesoscale for such a homogenized material response to become dominant.

theory, can - as an alternative - produce more realistic results than J_2 -plasticity. It is of interest to determine whether isotropic micropolar and micromorphic models can provide an alternative to physically based crystal plasticity models *on suitable length scales*, which are, however, yet to be determined.

3 Synthetic vs. experimental nanoindentation: a formal comparison

In this section, we illustrate the geometry of the relaxed-polar mechanism [12, 13, 33] in the setting of an idealized nanoindentation experiment. The deformation gradient F at a point and the material constants μ and μ_c enter as parameters and generate a pitchfork bifurcation, see [12, Fig. 3.1]. One makes the crucial observation that the classical continuum rotation $\text{polar}(F)$ is always a critical point, but not necessarily a minimizer for (1.1). In fact, in the non-classical regime $F \in D_{\mu, \mu_c}^{\text{NC}}$, $\text{polar}(F)$ turns into a local maximum. Only in this situation, the energy-minimizing branches $\text{rpolar}_{\mu, \mu_c}^+(F)$ and $\text{rpolar}_{\mu, \mu_c}^-(F)$ deviate from the polar decomposition and generate *non-classical* rotation patterns.

These non-classical Cosserat microrotation patterns motivated us to carry out a comparison with nanoindentation experiments which are known to produce non-classical rotation patterns below the indentation profile; in particular so-called *counter-rotations*. To be more precise, we compare the lattice orientation angles measured by 3D-EBSD analysis in [53] with the planar spin $\alpha(\text{rpolar}_{1,0}^\pm(F))$, see Definition 3.4 below, which is induced by the energy-minimizing Cosserat microrotation fields for a synthetic nanoindentation. To this end, we have constructed an explicit deformation mapping $\varphi_{\text{nano}} : \Omega \rightarrow \Omega_{\text{def}}$ which reveals the non-classical branch of $\text{rpolar}_{1,0}^\pm(F)$.

Remark 3.1 (Choice of the Cosserat couple modulus). *There are strong indications that a zero Cosserat coupling modulus $\mu_c = 0$ is the most interesting choice, first and foremost if one is interested in modeling a non-classical physical regime [27]. We mostly focus our attention on this particular choice in what follows. For a quite extensive discussion of the expected effects due to the choice of a strictly positive Cosserat coupling modulus $\mu_c > 0$, we refer the reader to [12].*

3.1 Nanoindentation in copper single crystals and 3D-EBSD analysis

In [8, 51–53] Zafarani et al. and in [44] Roters et al. reported on the orientation patterns below the indentation profiles of nanoindentations in copper single crystals. The lattice orientations in the deformed specimen were measured by three-dimensional **e**lectron **b**ackscatter **d**iffraction (3D-EBSD) analysis. Significant deviations of the local lattice orientations from the macroscopic continuum rotation have been observed and documented.¹¹ For a detailed description of 3D-EBSD and the sophisticated setup of the specific experiments considered here, we have to refer the interested reader to [53] and the doctoral dissertation of Zafarani [51]. Details of the focussed ion–beam–based experimental serial sectioning approach are given in [54].

A major motivation in [53] was to compare nanoindentation experiments carried out with a conical indenter with simulation results obtained with a physically-based crystal plasticity model introduced in [21, 22]. This model class tries to capture the crystal nanomechanics explicitly. Similarly, in our present exposition, we want to compare experimental observations with the relaxed-polar mechanism $\text{rpolar}_{1,0}^\pm(F)$.

Since our exposition contains figures from [53], we want to introduce some standard terminology from the material sciences and some physical properties of the copper crystal lattice. Solid copper has a face-centered (fcc) cubic crystal lattice, as illustrated in Figure 3.1. We employ the *Miller index notation*, which is based on integer crystal coordinates defined relative to a fixed choice of *unit cell*. By convention negative numbers are notated with a bar $\bar{n} := -n, n \in \mathbb{N}$. A unit cell of a three-dimensional crystal lattice is spanned by *direct lattice vectors*, e.g., $a_i \in \mathbb{R}^3, i = 1, 2, 3$, and contains a set of representative lattice points. The lattice points correspond to atom sites and an infinite (mathematical abstraction of a) crystal lattice is generated by all possible integer

¹¹From a modelling standpoint, this suggests to model the crystal lattice locally as an independent field of microrotations $R \in \text{SO}(3)$.

translations of the lattice points in the unit cell along the direct lattice vectors a_i . Each lattice point can be identified with a *crystal direction* $[hkl]$. For a cubic unit cell, e.g., a face-centered cubic copper single crystal, the lattice vectors a_i , $i = 1, 2, 3$, span a cube. Hence, the dual basis of (crystallographic) reciprocal lattice vectors a_i^* can be identified with the direct lattice vectors. In this particular case, the coefficients of a *crystal plane* (hkl) in Miller index notation can be interpreted as the coefficients of the associated normal vector (h, k, l) expressed in the basis of direct lattice vectors.¹²

It is well-known that dislocation glide is a major deformation mechanism in crystal mechanics. Dislocation glide occurs in a *slip system* (also glide system) which is a pair (P, L) of a two-dimensional glide plane $P \subset \mathbb{R}^3$ and a one-dimensional glide direction $L \subset P$ contained in the plane P .¹³ Note that in an fcc-crystal, one has, e.g., the family of glide planes $\{111\}$. The representative glide plane (111) and the crystal direction $[\bar{1}\bar{1}0]$ are an example for a slip system $(111)[\bar{1}\bar{1}0]$.¹⁴

The first slip system to be activated in a given mechanical process is referred to as the *primary slip system*. In practice, multiple slip systems can be active at the same time. In the series of experiments which we are interested in [53, Fig. 13], the pair $(111)[\bar{1}\bar{1}0]$ is the primary slip system. A suitable basis to study this particular system is given by crystal directions $[111]$, $[\bar{1}\bar{1}0]$ and $[11\bar{2}]$; see Figure 3.1.

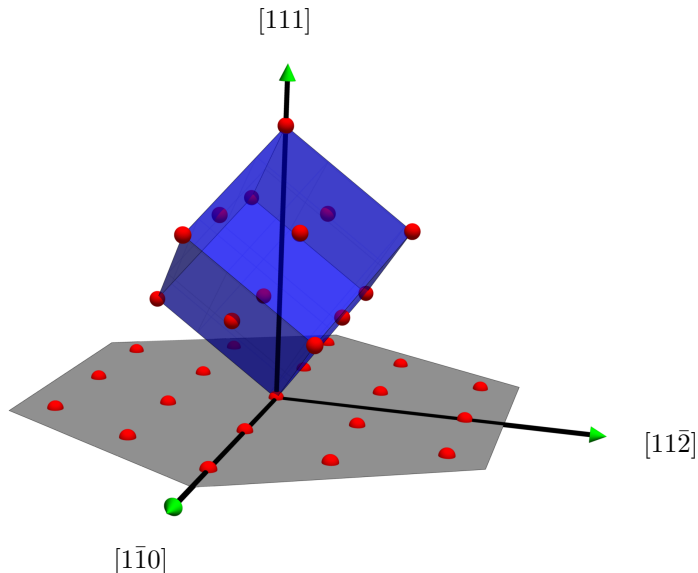


Figure 3.1: Illustration of an fcc (face-centered cubic) crystal lattice made up of copper atoms (red), a unit cell (blue) and the (111) crystal plane. The $[11\bar{2}]$ direction is perpendicular to the primary slip system $(111)[\bar{1}\bar{1}0]$. In [53], Zaafarani et al. carried out nanoindentation experiments with indentation direction $[111]$ and EBSD section planes parallel to the $(11\bar{2})$ crystal plane.

Consider a cubic crystal lattice spanned by a right-handed system of orthonormal direct lattice vectors $(a_1, a_2, a_3) \in \text{SO}(3)$ in two different orientations $R_a, R_b \in \text{SO}(3)$. This situation arises, e.g., if two different grains share a common grain boundary. The following is an intuitive

Definition 3.2 (Misorientation). *The misorientation between the lattice orientations $R_a, R_b \in \text{SO}(3)$ is given by*

$$R^{\text{mis}}(R_a, R_b) := R_b R_a^{-1} = R_b R_a^T \in \text{SO}(3).$$

Note that due to the point symmetries of the crystal lattice there are always multiple equivalent orientations of the lattice. The minimum over all possible misorientations is called the *disorientation*; cf. [51, Appendix E], or [43, p. 281] for an introduction.

¹²In general, a crystal plane is defined in terms of the dual basis a_i^* .

¹³Glide planes are crystal planes of closest two-dimensional atomic packings and glide directions are crystal directions characterized by closest one-dimensional packings.

¹⁴A family of planes is generated by the action of the space group \mathcal{G}_S on a representative crystal plane, here (111) . The space group \mathcal{G}_S is the group of affine linear maps which leave the lattice invariant.

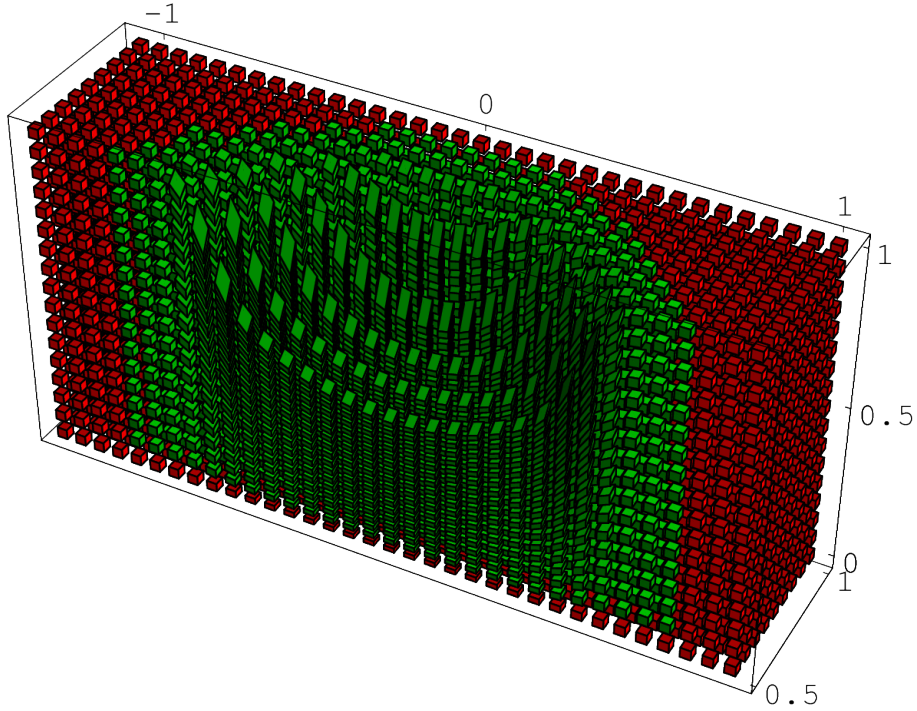


Figure 3.2: Illustration of the synthetic deformation $\varphi_{\text{nano}} : \Omega \rightarrow \Omega_{\text{def}}$. The action of the pointwise affine linear approximation $\varphi_{\text{nano,aff}}(p, h) = \varphi_{\text{nano}}(p) + F_{\text{nano}}(p)h$ is evaluated on a grid of small cubes. Only a part $\{(x, y, z)^T \in \Omega_{\text{def}} \mid y \geq 0.5\}$ of the deformed configuration is shown in order to reveal the cross-section $y = 1/2$. In the cylindrical inner part (green), the fields $\text{rpolar}_{1,0}^{\pm}(F)$ are strictly non-classical and deviate from the classical continuum rotation $\text{polar}(F)$.

In order to get a feeling for the spatial resolution of 3D-EBSD analysis and also for the length scale of the experiments, we now relate the size of a copper crystal lattice to the size of 3D-EBSD measurement points. The current estimate for the theoretical limit of the spatial resolution of 3D-EBSD measurements is $50 \times 50 \times 50 \text{ nm}^3$. Currently, a realistic resolution is $100 \times 100 \times 100 \text{ nm}^3$. The atomic radius for copper can be experimentally determined to be approximately $135 \text{ pm} = 1.35 \times 10^{-10} \text{ m} = 1.35 \text{ \AA}$. Further, the lattice constant for a solid copper crystal at room temperature has been determined as $\|a_i\| = a = 3.597 \pm 0.004 \text{ \AA}$; cf. [7]. This defines the sidelength of a unit cell of the lattice. Let us divide the sidelength of a 3D-EBSD voxel by the lattice constant a in order to compute the number of crystal unit cells per side of a 3D-EBSD measurement voxel. At a 100 nm resolution, this yields $\lfloor 100 \text{ nm} / 3.597 \text{ \AA} \rfloor = 278$ unit cells along each side of a voxel. Thus, *each single measurement point* of the lattice orientation field in the deformed specimen contains approximately $278^3 = 21\,484\,952$ unit cells, already at such an extremely fine resolution. We conclude that 3D-EBSD experiments extract misorientation mappings on a meso-scale which *might* be coarse enough to produce dominant deformation modes characterized by meso-mechanisms. By a meso-mechanism, we mean a mechanism which arises from the superposition of the collective deformation and rotation behavior associated with an underlying group of deformation carriers, i.e., dislocations in the current case, which are generated on a smaller scale and closely related to the specific crystal lattice. Let us suppose that such dominant meso-mechanisms do exist; then the consequences are two-fold: first, the question arises how closely the meso-mechanism is still related to the crystal lattice structure which generates it; second, since the results are homogenized, they can be compared with simulations based on continuum mechanical models. It might even be possible to approximate a dominant meso-mechanism phenomenologically without introducing the fundamental crystal mechanics which generate it. From this perspective, our interest is to determine, whether the relaxed-polar mechanism possibly allows to (approximatively) describe a known meso-mechanism: the counter-rotation patterns in nanoindentation.

3.2 Construction of a synthetic nanoindentation

Currently there is no experimental technique which allows to obtain the time-dependent deformation mapping $\varphi_{\text{exp}}(t, \cdot) : \Omega \rightarrow \Omega_{\text{def}}(t)$, $t \in [0, T]$, from the material sample during a nanoindentation experiment. The 3D-EBSD technique measures the misorientation R^{mis} of the lattice structure after the indentation process has completed. To understand the development of rotation patterns, one typically varies the applied loading in a sequence of indentations. Due to the sectioning process it is, however, currently not possible to obtain the time-dependent misorientation map $R^{\text{mis}}(t, \cdot)$ for a *single* nanoindentation process. Thus, there are still many open questions regarding the precise physical unfolding of the actual deformation process encoded by $\varphi_{\text{exp}}(t, \cdot)$ in the crystalline specimen which induces the final state of the misorientation pattern $R^{\text{mis}}(T, \cdot)$ as measured by the 3D-EBSD technique. In other words, it is not entirely clear, how the lattice misorientation patterns precisely develop in time into their final structure, as documented, e.g., in Figure 3.6 and [53].

Since the deformation mapping $\varphi_{\text{exp}}(t, \cdot)$ for a nanoindentation experiment cannot be measured yet (only the misorientation), we shall content ourselves with the study of an explicitly prescribed deformation mapping $\varphi_{\text{nano}} : \Omega \rightarrow \Omega_{\text{def}}$. The parametrization of φ_{nano} , given below, models the deformation of the sample after unloading of the indenter at final time T of an experiment and qualitatively matches the profile of a nanoindentation in [53].¹⁵ For the reference configuration of the synthetic nanoindentation, we choose $\Omega = \{(x, y, z)^T \in \mathbb{R}^3 \mid \|(x, y, z)^T\|_\infty < 1\}$, which is a cube in \mathbb{R}^3 centered about the origin. This can be considered as a nondimensionalized sample. In the experiments a conical indenter was used which has rotational symmetry. This symmetry is also respected by our proposed deformation φ_{nano} .

We now list some shortcomings of our synthetic nanoindentation φ_{nano} : first of all, the deformation mapping φ_{nano} is not a solution to a Cosserat boundary value problem, it is just a mapping which suitably displaces points vertically, i.e., from top to bottom, to create an indentation profile. In particular, there is no horizontal transport of matter. Further, we have confined the deformation φ_{nano} to a cylinder with radius 1. This implies that the typical formation of pile-up patterns around the indentation profile, as investigated, e.g., in [50, 55–57], is not accounted for by the synthetic nanoindentation φ_{nano} .¹⁶

Let us now state the explicit parametrization of $\varphi_{\text{nano}} : \Omega \rightarrow \Omega_{\text{def}}$ on which our subsequent computations and our formal comparison are based. Setting $r(x, y)^2 := x^2 + y^2$, we introduce

$$\varphi_{\text{nano}}(x, y, z)^T = \begin{cases} \left(x, y, \frac{3z}{4} \left(r^2 + \frac{1}{3}\right)\right) & , \text{ if } 0 \leq r \leq \frac{1}{2} \\ \left(x, y, z \left(1 + \frac{3}{4} \frac{r^2 - 1}{\exp\left(\frac{1}{1-r} + \frac{2}{1-2r}\right) + 1}\right)\right) & , \text{ if } \frac{1}{2} < r < 1 \\ (x, y, z) & , \text{ otherwise .} \end{cases}$$

For the construction of the mapping $\varphi_{\text{nano}} : \Omega \rightarrow \Omega_{\text{def}}$, we proceed as follows:¹⁷

$$f(t) := \begin{cases} \exp(-t) & , \text{ if } t > 0 \\ 0 & , \text{ otherwise} \end{cases} , \quad (3.1)$$

$$g(r; a, b) := \frac{f(b-r)}{f(b-r) + f(r-a)} , \quad (3.2)$$

$$h(x, y, z) := z \left(1 - \frac{3}{4}(1-r^2)g\left(r; \frac{1}{2}, 1\right)\right) , \quad \text{and} \quad (3.3)$$

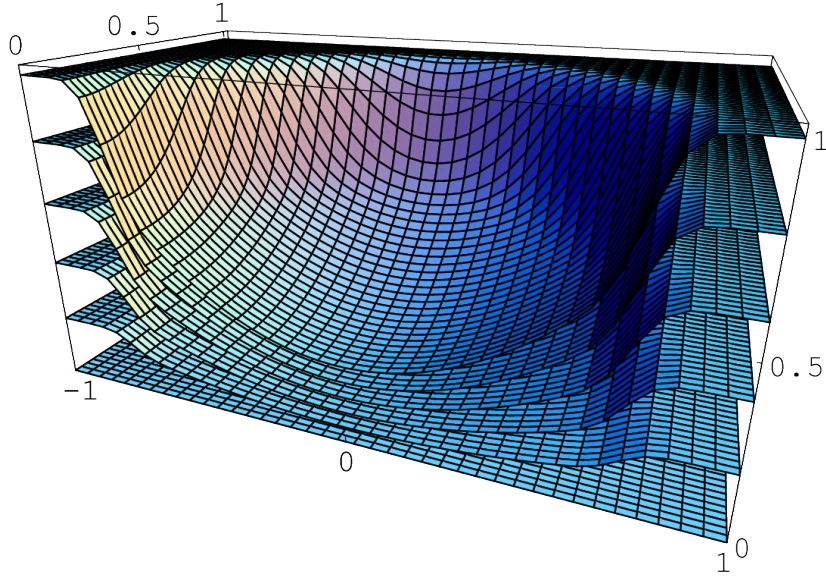
$$\varphi_{\text{nano}}(x, y, z)^T := (\text{id}_{\mathbb{R}^2}(x, y), h(x, y, z)) = (x, y, h(x, y, z)) . \quad (3.4)$$

Note that φ_{nano} is an orientation preserving diffeomorphism, i.e., the deformation gradient field $F_{\text{nano}} : \Omega \rightarrow \Omega_{\text{def}}$ takes values in $\text{GL}^+(3)$.

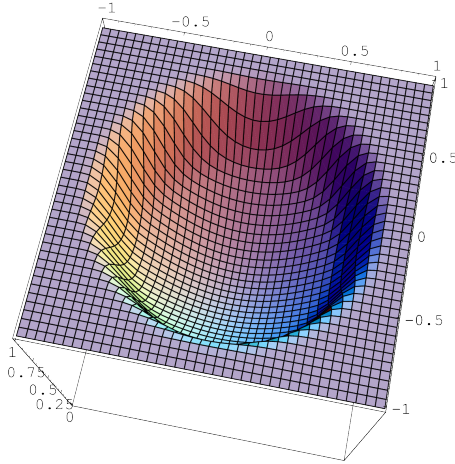
¹⁵Note that a realistic deformation mapping induced by a nanonindentation experiment $\varphi_{\text{exp}}(t, \cdot)$ is certainly far more complicated than φ_{nano} . However, the reduced complexity is advantageous for the exposition of the relaxed-polar mechanism.

¹⁶We expect that pile-up patterns are produced by the solution of the *isotropic Cosserat boundary value problem*, i.e., the variational problem (2.18) for realistic boundary conditions. However, these pile-up patterns cannot be expected to correlate with a particular crystal structure unless one enhances the elastic energy and the hardening contributions to model the anisotropy. As a first step, we can introduce a contribution $\langle \mathbf{C} \cdot \log U_e, \log U_e \rangle$, where \mathbf{C} denotes the anisotropic fourth order linear elasticity tensor. To model an anisotropic material response which is more realistic at the nanometer length scale, one may couple the Cosserat model to a suitable single crystal plasticity model.

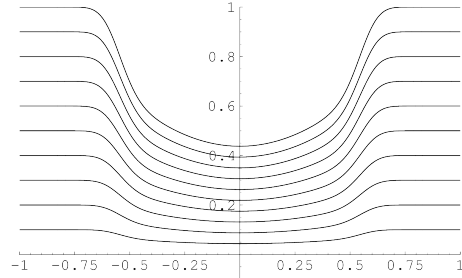
¹⁷The construction uses a well-known bump function for the construction of a smooth partition of unity.



(a) Deformation of layers parallel to the xz -plane.



(b) Top view of indentation.



(c) Layers in the section plane $y = 1/2$.

Figure 3.3: Visualization of the parametrization of the indentation profile modelled by φ_{nano} . The coloring has no quantitative meaning and the units are not specified since the construction is nondimensionalized.

The construction is rotationally symmetrical. Introducing cylindrical coordinates (r, ϑ, h) with respect to both, the reference and the deformed configuration, the deformation gradient is easily seen to have the following form

$$F_{\text{nano}}(r, \vartheta, h) = D_{(r, \vartheta, h)} \varphi_{\text{nano}}(r, \vartheta, h) = \begin{pmatrix} 1 & 0 & 0 \\ 0 & 1 & 0 \\ (\partial_r \varphi_{\text{nano}})(r, h) & 0 & (\partial_h \varphi_{\text{nano}})(r, h) \end{pmatrix}. \quad (3.5)$$

In particular, since $\partial_{\vartheta} \varphi_{\text{nano}} = 0$ the deformation gradient is independent of ϑ . The cylindrical symmetry in radial cross sections with constant values of ϑ allows us to visualize some properties of the synthetic indentation φ_{nano} in the plane $\vartheta = 0$ (which coincides with the cartesian xz -plane). This radial symmetry is also reflected in the fields of relaxed polar factors $\text{rpolar}_{1,0}^{\pm}(F_{\text{nano}})$ and the continuum rotation $\text{polar}(F_{\text{nano}})$.

In order to give the reader an impression how $\varphi_{\text{nano}} : \Omega \rightarrow \Omega_{\text{def}}$ deforms the idealized specimen Ω , we have visualized the local action of the deformation gradient field $F_{\text{nano}} := \nabla \varphi_{\text{nano}}$ in Figure 3.2 and Figure 3.4. The action of φ_{nano} on layers parallel to the xz -plane is illustrated in Figure 3.3.

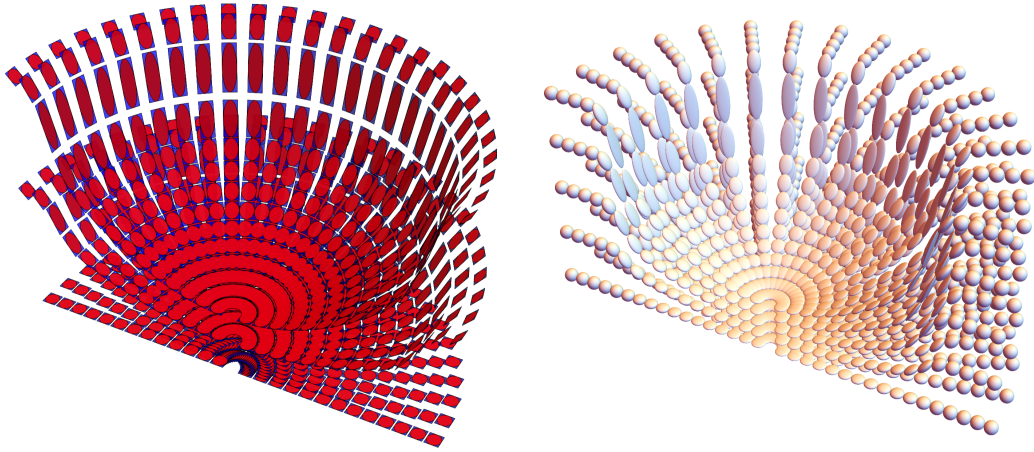


Figure 3.4: *Left*: Visualization of the plane of maximal stretch $P_{\text{def}}^{\text{ms}}(F_{\text{nano}})$ [blue] for the synthetic nanoindentation (in the deformed configuration) scaled to match the intersection with the stretch ellipsoid [red]. *Right*: Field of stretch ellipsoids for φ_{nano} . Note how $\text{polar}(F) \in \text{SO}(3)$ makes the stretch ellipsoids tumble symmetrically into the indentation. The coloring has no quantitative meaning.

3.3 Fields of energy-minimizing Cosserat rotations $\text{rpolar}_{1,0}^{\pm}(F)$

In our introduction, we present the explicit form of the two energy-equivalent optimal Cosserat rotations $\text{rpolar}_{1,0}^{\pm}(F)$ derived in [13]. The construction is pointwise and depends on a choice of an orthonormal eigensystem $Q \in \text{SO}(3)$ of U (or C , respectively). In order to synthetically reproduce the nanoindentation experiments due to Raabe et al. with our previously described φ_{nano} , we have to extend our definition from a pointwise one to a field version of $\text{rpolar}_{1,0}^{\pm}(F)$. To this end, we need to construct an *eigenframe* for U , i.e., a field $Q : \Omega \rightarrow \text{SO}(3)$ which diagonalizes $U = QDQ^T$ pointwise.

It is desirable to compute an extension which is as regular as possible, since, in the full variational model (2.18), the gradient of the microrotation field R is regularized by the Cosserat curvature term $\|R^T \text{Curl } R\|^2$. However, a regular field extension, e.g., a continuous one, is more difficult to obtain than one might think at first glance. The main reason is that the pointwise numeric eigendecomposition of U often yields a discontinuous field of principal directions, mostly due to jumps in eigenspace orientations.¹⁸

We now state our procedure for the computation of an eigenframe in

Remark 3.3 (A simple strategy for the computation of Q). *Let $F := \nabla \varphi_{\text{nano}}$ and suppose that $U := \sqrt{F^T F} \in \text{Sym}^+(3)$ has only distinct eigenvalues. Furthermore, let $v_1, v_2, v_3 \in \mathbb{R}^3$ with $\|v_i\| = 1$, $i = 1, 2, 3$, be a numerically computed eigensystem of U . Ignoring issues of numerical stability, we have $V = (v_1 | v_2 | v_3) \in \text{O}(3)$, since the eigenspaces of U are pairwise orthogonal. For positively oriented $V \in \text{SO}(3)$, we can set $Q = V$. Otherwise, we fix the orientation by reflecting the last column, i.e., $Q = (v_1, v_2, -v_3) \in \text{SO}(3)$. This yields a positively oriented eigenframe diagonalizing $U = QDQ^T$.*

The fields $\text{rpolar}_{1,0}^{\pm Q}(F)$ illustrated in our various figures have all been computed using the above strategy; cf. also the implementation provided in Appendix A.

¹⁸Note that there are also topological constraints. To give an example, let us embed a smooth surface $S \subset \Omega$ which is homeomorphic to the two-sphere \mathbb{S}^2 and restrict $Q|_S$. Suppose that the first column $q_1 : S \rightarrow TS$ is continuous. Then the well-known “hairy ball theorem” (see, e.g., [20, p. 382, Ex. 14-22]) implies $q_1(p) = 0$ in at least one point $p \in S$. This contradicts $\|q_1\| = 1$.

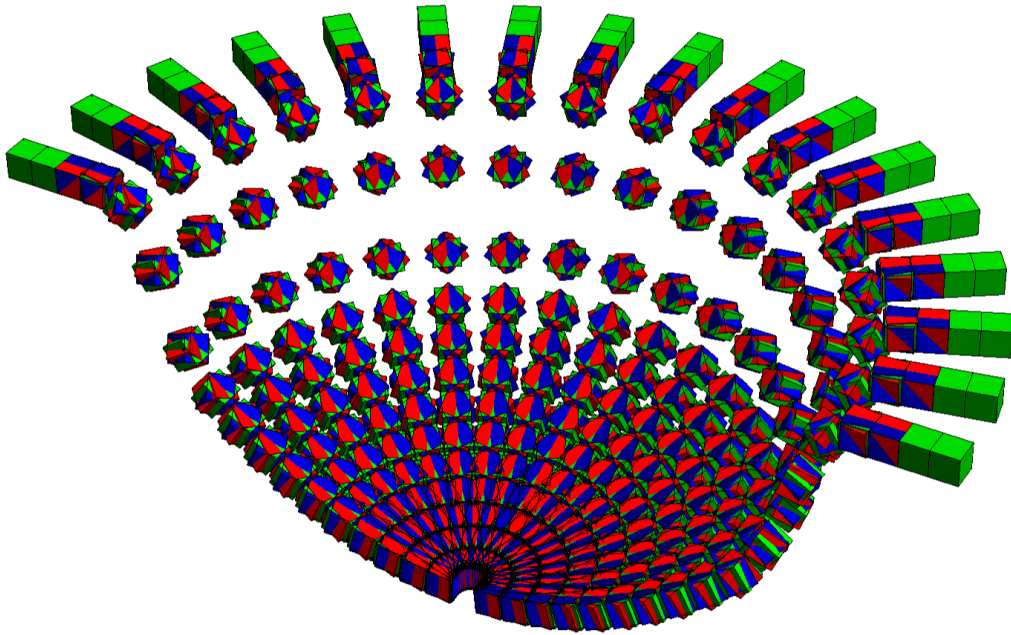


Figure 3.5: Action of rotation fields on radially aligned “infinitesimal” cubes; the classical macroscopic continuum rotation $\text{polar}(F_{\text{nano}})$ [green] tilts the cubes inwards into the indentation and respects the rotational symmetry. In strong contrast, the relaxed polar factors $\text{rpolar}_{1,0}^+(F_{\text{nano}})$ [red] and $\text{rpolar}_{1,0}^-(F_{\text{nano}})$ [blue] rotate the cubes out of the radial symmetry planes of φ_{nano} . Note the inconsistency slightly right off the middle [red/blue] which illustrates a flip of the two optimal branches $\text{rpolar}_{1,0}^\pm(F)$. This is due to an instability of the subspace orientation in the computation of the eigenframe Q for U .

3.4 The planar spin as a measure for counter-rotations in a plane

In certain experiments in structural mechanics, e.g., in micro- and nanoindentations, but also in natural phenomena, e.g., certain types of ground slides, one repeatedly observes non-classical rotation patterns in the particular form of *counter-rotations*. These can take the form of local rotations in the opposite sense of the continuum rotation $\text{polar}(F) \in \text{SO}(3)$. We invite the reader to imagine a pair of counter-rotating vortices which develop in his hot morning coffee (or tea) with a little bit of milk, excited with a linear motion of the spoon.¹⁹

Thus we require a measure for the amount of rotation in a section plane that is induced by the deformation $\varphi : \Omega \rightarrow \Omega_{\text{def}}$. More precisely, we want to measure how much the deformation gradient field $F := \nabla\varphi$ locally rotates the specimen Ω in an oriented section plane (Σ, n) . This will also allow us to quantify the notion of counter-rotations in a plane. To this end, we introduce the notion of an (*apparent*) *planar spin* induced by a linear mapping $L \in \mathbb{R}^{3 \times 3}$ in a given oriented affine section plane $(\Sigma + p, n)$, where $n \in \mathbb{S}^2$ is a unit normal vector, $\Sigma = n^\perp$, and $p \in \mathbb{R}^3$. For the current exposition, it suffices to assume $p = 0$. Moreover, in this case, the oriented section plane can be identified with its normal vector n .

Let $\text{SO}(3)_n := \{R \in \text{SO}(3) \mid Rn = n\} < \text{SO}(3)$ be the subgroup of rotations with fixed axis of rotation given by $\text{span}(\{n\})$ and note that the rotations in $\text{SO}(3)_n$ leave the oriented section plane (Σ, n) fixed. The direction vector $n \in \mathbb{S}^2$ equips the rotation axis $\text{span}(\{n\})$ with an orientation. This allows to identify a rotation $R_n \in \text{SO}(3)_n$ with a unique signed rotation angle $\alpha \in (-\pi, \pi]$.

¹⁹There is also a notion of an *elastic* vortex. Recent simulations based on the so-called “movable cellular automata method” [42] model internal friction and show interesting results in contact loadings, i.e., counter-rotations, see [47, p. 3]. Note that there are interesting connections to Cosserat theory which might even be recovered as a continuum limit of the method.

As a preparation for our next definition, we recall the parametrization for a planar rotation

$$\check{R} : (-\pi, \pi] \rightarrow \text{SO}(2), \quad \check{R}(\alpha) := \begin{pmatrix} \check{R}_{11} & \check{R}_{12} \\ \check{R}_{21} & \check{R}_{22} \end{pmatrix} = \begin{pmatrix} \cos(\alpha) & -\sin(\alpha) \\ \sin(\alpha) & \cos(\alpha) \end{pmatrix} \in \text{SO}(2).$$

From this, it is easy to see that the inverse mapping is well-defined and given by

$$\check{\alpha} : \text{SO}(2) \rightarrow (-\pi, \pi], \quad \check{\alpha}(\check{R}) := \text{sign}(\check{R}_{21}) \arccos(\check{R}_{11}).$$

Related notions such as the lattice disorientation angle in texture analysis (see, e.g., [43]), suggest to associate a signed rotation angle with $L \in \mathbb{R}^{3 \times 3}$ as a means to measure the apparent rotation due to L in the oriented plane (Σ, n) . Our present approach to compute this angle is based on a (nonlinear) best approximation of L by a rotation with fixed rotation axis $R_n(L) \in \text{SO}(3)_n \cong \text{SO}(2)$ and with respect to the Frobenius matrix norm. This amounts to the solution of

$$R_n(L) := \arg \min_{\substack{R \in \text{SO}(3) \\ Rn = n}} \|L - R\|^2. \quad (3.6)$$

In a second step, we extract the signed rotation angle from this ‘‘closest’’ rotation $R_n(L)$.²⁰

Given $Q \in \text{SO}(3)$, such that $Qe_3 = n$, we can consider the oriented section plane defined by $(\Sigma = \text{span}(\{q_1, q_2\}), q_3)$ and find that $R \in \text{SO}(3)_n$ can be parametrized by

$$R(\alpha) = Q \begin{pmatrix} \cos(\alpha) & -\sin(\alpha) & 0 \\ \sin(\alpha) & \cos(\alpha) & 0 \\ 0 & 0 & 1 \end{pmatrix} Q^T. \quad (3.7)$$

Hence, the problem (3.6) reduces to finding a closest planar rotation from

$$R_n(L) := \arg \min_{\substack{R \in \text{SO}(3) \\ Rn = n}} \|L - R\|^2 = Q \left\{ \arg \min_{\check{R} \in \text{SO}(2)} \left\| Q^T L Q - \begin{pmatrix} \check{R} & 0 \\ 0 & 1 \end{pmatrix} \right\|^2 \right\} Q^T. \quad (3.8)$$

Only the upper left 2×2 block varies under different values of the rotation \check{R} . Introducing

$$\check{L}_n(L) := \begin{pmatrix} (Q^T L Q)_{11} & (Q^T L Q)_{12} \\ (Q^T L Q)_{21} & (Q^T L Q)_{22} \end{pmatrix}, \quad (3.9)$$

it suffices to solve the two-dimensional problem

$$\check{R}_n(L) := \arg \min_{\check{R} \in \text{SO}(2)} \|\check{L}_n(L) - \check{R}\|^2. \quad (3.10)$$

For the sake of completeness, we want to mention that the original spatial rotation $R_n(L) \in \text{SO}(3)_n$ can be uniquely recovered from the solution $\check{R}_n(L)$ to the planar problem (3.10).

Assuming that $\check{L} \in \text{GL}^+(2)$, Grioli’s theorem shows that the unique best approximation \check{R}_n with respect to the Frobenius matrix norm is the polar factor $\text{polar}(\check{L}) \in \text{SO}(2)$. Most conveniently, an explicit expression for $\text{polar}(\check{L})$ is available in dimension $n = 2$. Moreover, for all $n > 1$, the best approximation can be shown to coincide with those for the geodesic distance on $\text{SO}(n)$ equipped with its natural bi-invariant Riemannian metric. In particular, we have [19, 39]

$$\text{polar}(\check{L}) = \arg \min_{\check{R} \in \text{SO}(2)} \text{dist}_{\text{euclid}}(\check{L}, \check{R}) = \arg \min_{\check{R} \in \text{SO}(2)} \text{dist}_{\text{geod}}(\check{L}, \check{R}). \quad (3.11)$$

Although the closest rotation (best approximation) is the same for both the extrinsic (euclidean) and the intrinsic (Riemannian) distance measure, the minimal distance (approximation error) itself is different.

The preceding development motivates

²⁰This is a distance problem in $\mathbb{R}^{3 \times 3}$ with respect to the euclidean distance measure $\text{dist}_{\text{euclid}}(X, Y) := \|Y - X\|$ induced by the Frobenius matrix norm.

Definition 3.4 (The planar spin). *Let $L \in \text{GL}^+(3)$ and $\check{L}(L) \in \text{GL}^+(2)$ as before, then*

$$\check{R}_n(L) := \arg \min_{\check{R} \in \text{SO}(2)} \|\check{L}_n(L) - \check{R}\|^2. \quad (3.12)$$

The **planar spin** induced by L in the oriented section plane (Σ, n) is

$$\alpha_n : \text{GL}^+(3) \rightarrow (-\pi, \pi], \quad \alpha_n(L) := \check{\alpha}(\check{R}_n(\check{L}_n)). \quad (3.13)$$

Although Q is not uniquely defined in the definition of \check{L}_n , the planar spin $\alpha_n(L)$ is well-defined since rotations about the same axis n always commute.

Example 3.5. *Let $(\Sigma, n) = (\text{span}(\{e_1, e_2\}), e_3)$ and $L \in \mathbb{R}^{3 \times 3}$. Further, we denote the upper left 2×2 block of L by \check{L} . In this case, we have $n = e_3$ and $Q = \mathbf{1}$ and we find*

$$R_n(L) = \begin{pmatrix} \check{R}_n(L) & 0 \\ 0 & 1 \end{pmatrix}.$$

Thus, with the explicit form of the polar decomposition in dimension $n = 2$ (see, e.g., [11]), we obtain

$$\check{R}_n(L) = \text{polar}(\check{L}) = \frac{1}{\sqrt{\|\check{L}\|^2 + 2 \det[\check{L}]}} \begin{pmatrix} -(\check{L}_{11} + \check{L}_{22}) & \check{L}_{12} - \check{L}_{21} \\ \check{L}_{21} - \check{L}_{12} & -(\check{L}_{11} + \check{L}_{22}) \end{pmatrix}. \quad (3.14)$$

Remark 3.6 (Approximation error of the planar spin). *A best approximation is only guaranteed to be a good approximation if the associated approximation error is small. This need not be the case for the proposed planar spin measure $\alpha_n(L)$. Intuitively spoken, the measured effects coincide with our expectations if $L \in \mathbb{R}^{3 \times 3}$ essentially acts only in the section plane (Σ, n) . On the other extreme, if L is a rotation about an axis $d \perp n$, i.e., $d \in \Sigma$, the planar spin degenerates. We may even conclude that the observation of counter-rotations in a section plane which does not conform well with the actual mechanical workings that happen during the deformation of the specimen, may in fact be misleading our intuition.*

3.5 A formal comparison of rotation patterns in experimental and synthetic nanoindentation

We are now in the position to present a formal comparison of the non-classical rotation patterns arising in real nanoindentation experiments below the indentation profile which we oppose with the planar spin $\alpha(\text{rpolar}^\pm(F_{\text{nano}}))$ due to our synthetic nanoindentation φ_{nano} .

In Figure 3.6 and Figure 3.8 (courtesy of Raabe et al.), we show 3D-EBSD measurements of the crystal lattice misorientation after a series of nanoindentations in a copper single crystal [53]. The figures illustrate the experimentally obtained rotational deviation of the deformed lattice relative to its original state. More precisely, both, Figure 3.6 and Figure 3.8, display the lattice disorientation expressed as signed rotation angles relative to the $(11\bar{2})$ crystal plane; cf. [51, Appendix E]. Note the typical pattern of counter-rotations separated by multiple cross-over zones. Furthermore, comparisons with crystal-plasticity simulations based on a model due to [21, 22] are presented in Figure 3.6 which show favorable qualitative results.

For comparison, we show the planar spin $\alpha : \text{SO}(3) \rightarrow (-\pi, \pi]$ in the xz -plane which is oriented such that the sign of the rotation angles coincides with the usual convention for angles in the plane. We have computed this spin for the classical continuum rotation $\text{polar}(F_{\text{nano}})$ and the relaxed polar factors $\text{rpolar}_{1,0}^\pm(F_{\text{nano}})$ in Figure 3.7. Both plots show values attached to the deformed configuration. In order to indicate the rotation patterns that can be realized by a solution of a Cosserat boundary value problem, we have patched together the two branches of $\text{rpolar}_{1,0}^\pm(F)$ in a suitable way, see Figure 3.9. Note that the discontinuity in $x = 0$ can be resolved by a steep gradient in the microrotation field R which is highly localized. Similarly, we expect that more complicated rotation patterns can be realized as is typically expected from a diffuse interface model.²¹

To ease the comparison with the experimentally obtained lattice misorientation angles depicted in Figure 3.6, we have used a similar color map with the same domain $[-8^\circ, 8^\circ]$.

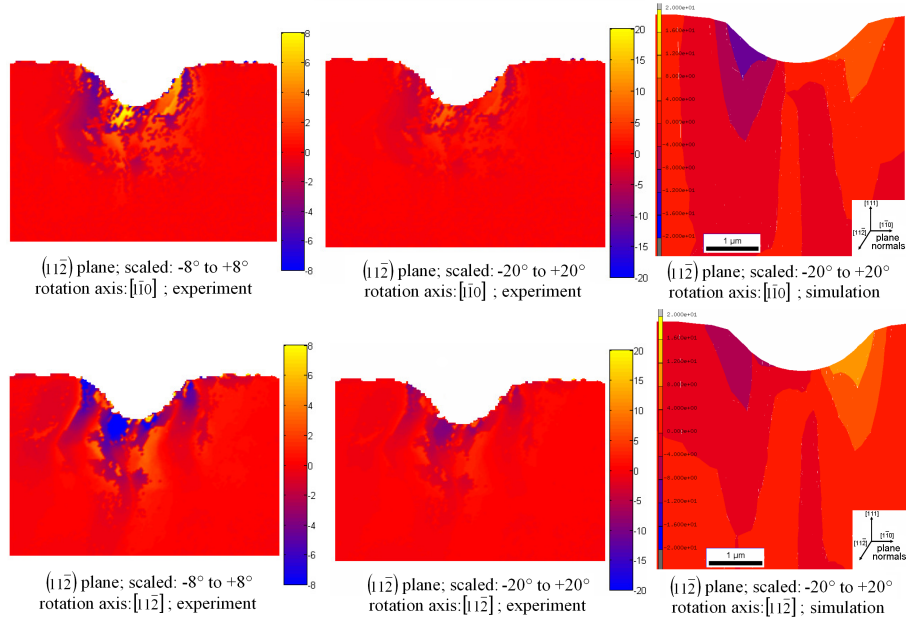


Figure 3.6: *Left*: Disorientation angle relative to the $[110]$ (top) and $[11\bar{2}]$ (bottom) crystal directions. The counter rotations correspond well with the planar spin in the section plane $y = 1/2$ induced by our synthetic indentation, see Figure 3.9. *Right*: Disorientation angle obtained by physics-based crystal plasticity simulations relative to the $[110]$ (top) and $[11\bar{2}]$ (bottom) rotation axes with a color scale ranging from $\pm 8^\circ$. (Reprint of [53, Fig. 13], with permission)

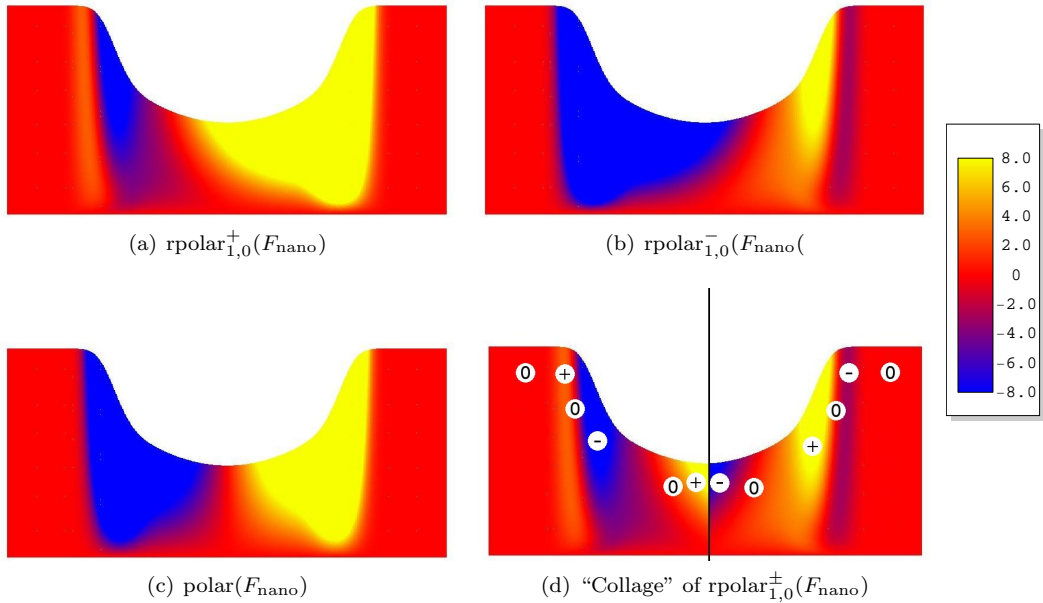


Figure 3.7: The planar spin $\alpha(F_{\text{nano}})$ in the intersection plane $y = \frac{1}{2}$ of $\text{rpolar}^\pm(F_{\text{nano}})$, an optimal choice of branches, and the continuum rotation $\text{polar}(F_{\text{nano}})$ with a color scale ranging through $[-8^\circ, 8^\circ]$. The section plane is parametrized by $(x, \frac{1}{2}, z)$ and the marks illustrate the sign of the planar spin and the cross-over points. *Note: the two outermost, slim zones of counter-rotations in the visualization may in fact be due to an instability of $\text{rpolar}_{1,0}^\pm(F)$ for $F \approx \mathbb{1}$. The large zones of counter-rotations are reliable.*

We summarize that the relaxed-polar mechanism $\text{rpolar}_{1,0}^\pm(F)$ is capable to produce non-classical

²¹The Cosserat curvature contribution can be interpreted as a regularization term in a diffuse interface approach for the field of microrotations R .

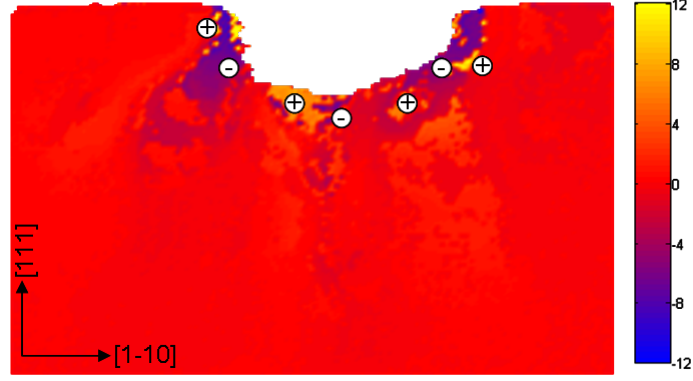


Figure 3.8: Rotation angles measured by 3D-EBSD analysis of a nanoindentation into a copper single crystal with a color map scaled to $\pm 8^\circ$. It is important to note the cross-over zones separating counter-rotations. The angles are computed with respect to the rotation axis $[11\bar{2}]$ for rotations in the $(11\bar{2})$ -plane (courtesy of Raabe et al., see, e.g., [53]).

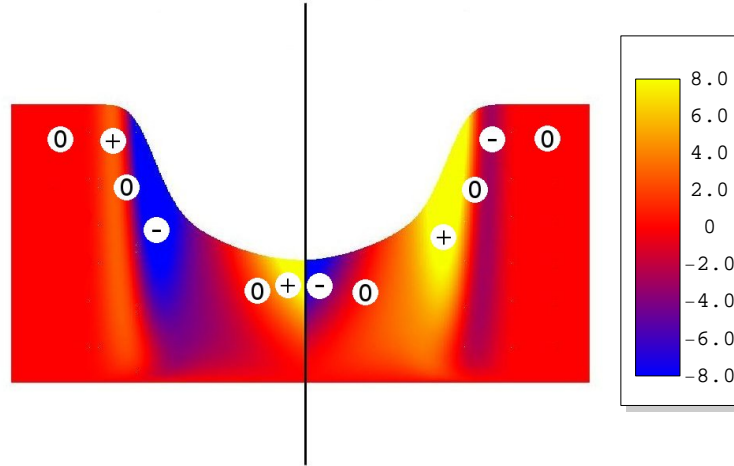


Figure 3.9: Planar spins $\alpha_{e_2}(\text{rpolar}_{1,0}^\pm(F))$ for the synthetic nanoindentation mapping φ_{nano} evaluated on the intersection with the $y = 1/2$ -plane. Note that both branches are patched together at $x = 0$ in order to illustrate the possibility of counter rotations. In the full boundary value problem (2.18), such discontinuities can be resolved by solutions with a steep gradient in the Cosserat microrotation field.

rotation patterns as opposed to the classical macroscopic continuum rotation $\text{polar}(F)$. Whether this mechanism can be successfully exploited for the realistic modelling of nanoindentations is open to future investigation. It seems to us that one cannot expect to obtain realistic results on the nanometer scale without incorporating the geometry of the crystalline material explicitly. However, the energy-optimal deformation modes related to the plane of maximal stretch $\text{P}^{\text{ms}}(F)$, see Figure 3.4 are very interesting on the right mesoscale. We imagine that the movement in glide planes is averaged at coarse enough length scales and that the material deforms rather freely in an arbitrary direction of maximal planar loading, although the deformation itself is realized by a complex super-position of dislocation glides respecting the crystal mechanics specific to the crystalline material.

4 Conclusion

In a series of nanoindentation experiments in copper single crystals described and analyzed in [8, 51–53], a formation of multiple typical zones of lattice rotations was observed. These rotation patterns are characterized by alternating signs of the field of lattice misorientation angles. We are mostly considered with orientation angles in the $(11\bar{2})$ crystal plane below the indentation profile. Physically based crystal plasticity simulations based on a model proposed in [21, 22] reproduced the rotation and pile-up patterns below the indentation profile quite well [51, 53]. The computed lattice misorientation angles were quantitatively slightly overestimated, but possible strategies to overcome this phenomenon by an improved treatment of dislocation effects are mentioned.

For the sole purpose of demonstrating failure of the method, Zaafarani carried out simulations based on an isotropic J_2 -plasticity model [51]. As expected, this approach did not reproduce the experimentally observed rotation zones. This motivated us to investigate whether an *isotropic* Cosserat model can produce more realistic rotation patterns.

In the present work, we have made another step forward in our ongoing analysis of the geometry of the isotropic geometrically nonlinear Cosserat model (2.18) with zero Cosserat couple modulus $\mu_c = 0$ which was originally proposed in the habilitation thesis of the second author [26]. Our analysis shows that the Cosserat model with $\mu_c = 0$ *is capable to produce non-classical rotation patterns* which are at least similar to observations in nanoindentation experiments [53]. This is only possible due to the additional field of Cosserat microrotations $R : \Omega \rightarrow \text{SO}(3)$. Note that the understanding of the effects that can be generated by the field of microrotations R is an important aspect of our efforts towards a deeper understanding of the variational Cosserat model. For now, we conclude that the energy-minimizing rotation fields $\text{rpolar}_{\mu,0}^{\pm}(F)$, i.e., with $\mu_c = 0$, do provide an interesting new mechanism.

Due to the isotropic modelling approach, one cannot expect to obtain realistic results representing the rich anisotropic material behavior which a copper crystal lattice can produce at the nanometer scale.²² Our present analysis of a synthetic nanonindentation and the direct comparison with measurements in a two-dimensional section shows that the rotation fields $\text{rpolar}_{1,0}^{\pm}(F_{\text{nano}})$ produce an interesting match, if we compose the two branches of $\text{rpolar}_{1,0}^{\pm}(F)$ in a suitable way. This composition is not superficial, since in the solution of a Cosserat boundary value problem, a mixture of the two branches is the *expected* result. In fact, such complex rotation patterns have already been observed in numerical Cosserat plasticity simulations by Blesgen, see [2–5].

We briefly report on possible future directions. It remains to be seen how the relaxed-polar mechanism discovered in our investigation of the perfectly spatially decoupled model with $L_c = 0$ in [12, 13, 33] is reflected in solutions to Cosserat boundary value problems. We also expect non-classical rotation patterns with essential features of $\text{rpolar}_{1,0}^{\pm}(F)$ in numerical solutions in both two and three space dimensions. It is an interesting question, whether these deviations are also realized in numerical simulations of the Cosserat model with $0 < L_c \ll 1$ (or even observable in experiments such as nanoindentation). This raises questions on how the solutions to the Cosserat boundary value problem with $L_c = 0$ and $0 < L_c \ll 1$ are precisely related. This is still an open problem. We expect that the relaxed-polar mechanism which stems from the investigation of the limit case without Cosserat curvature $L_c = 0$ plays an important part also for small length scales $0 < L_c \ll 1$.

Let us conclude this contribution with an interesting experimental observation with possible implications on the choice of material parameters in the Cosserat model.

Remark 4.1 (Counter-rotations at the onset of nanoindentation and zero Cosserat couple modulus $\mu_c = 0$). *The counter-rotation patterns forming during nanoindentation experiments are quite sensitive: they form right at the onset of the process, i.e., for very small indenter loads. A zero Cosserat couple modulus $\mu_c = 0$ introduces this kind of sensitivity in the Cosserat model as opposed to a strictly positive $\mu_c > 0$. In the latter case, the non-classical effects are only triggered once a certain threshold for the maximal mean planar strain $s^{\text{mmp}}(F)$ is exceeded [12, 13].*

²²Note that it is possible to modify the Cosserat model such that it includes anisotropic effects due to a particular crystal lattice structure.

5 Acknowledgments

A. Fischle is currently supported by German Research Foundation (DFG) grant SA2130/2-1 and has been partially supported by DFG grant NE902/2-1 (also: SCHR570/6-1). We thank our anonymous referees for their concise and inspiring remarks which helped us to improve the paper.

References

- [1] A. A. Benzerga, Y. Bréchet, A. Needleman, and E. van der Giessen. The stored energy of cold work: Predictions from discrete dislocation plasticity. *Acta Mater.*, 53(18):4765 – 4779, 2005. 9
- [2] T. Blesgen. Domain partitioning as a result of deformation in the framework of large-strain Cosserat plasticity. *arXiv preprint arXiv:1208.3331*, 2012. 24
- [3] T. Blesgen. Deformation patterning in the framework of large-strain Cosserat plasticity. *Model. Simul. Mater. Sc.*, 21(3):035001, 2013. 24
- [4] T. Blesgen. Deformation patterning in three-dimensional large-strain Cosserat plasticity. *Mech. Res. Comm.*, 62:37 – 43, 2014. 24
- [5] T. Blesgen. On rotation deformation zones for finite-strain Cosserat plasticity. *Acta Mech.*, 226(7):2421–2434, 2015. 24
- [6] E. Cosserat and F. Cosserat. *Théorie des Corps Déformables*. Librairie Scientifique A. Hermann et Fils (engl. translation by D. Delphenich 2007, available online at https://www.uni-due.de/~hm0014/Cosserat_files/Cosserat09_eng.pdf), reprint 2009 by Hermann Librairie Scientifique, ISBN 978 27056 6920 1, Paris, 1909. 2
- [7] W. P. Davey. Precision measurements of the lattice constants of twelve common metals. *Phys. Rev.*, 25:753–761, Jun 1925. 15
- [8] E. Demir, D. Raabe, N. Zaafarani, and S. Zaefferer. Investigation of the indentation size effect through the measurement of the geometrically necessary dislocations beneath small indents of different depths using EBSD tomography. *Acta Mater.*, 57(2):559 – 569, 2009. 7, 13, 24
- [9] O. Dmitrieva, P. W. Dondl, S. Müller, and D. Raabe. Lamination microstructure in shear deformed copper single crystals. *Acta Mater.*, 57(12):3439 – 3449, 2009. 11, 12
- [10] A. C. Eringen. *Microcontinuum Field Theories. Vol. I: Foundations and Solids*. Springer, 1999. 2
- [11] A. Fischle. The planar Cosserat model: minimization of the shear energy on $SO(2)$ and relations to geometric function theory. (diploma thesis). 2007. (available online: http://www.uni-due.de/~hm0014/Supervision_files/dipl_final_online.pdf). 21
- [12] A. Fischle and P. Neff. The geometrically nonlinear Cosserat micropolar shear–stretch energy. Part I: A general parameter reduction formula and energy-minimizing microrotations in 2D. *Z. Angew. Math. Mech.*, 97(7):828–842, 2017. 3, 5, 8, 11, 13, 24
- [13] A. Fischle and P. Neff. The geometrically nonlinear Cosserat micropolar shear–stretch energy. Part II: Non-classical energy-minimizing microrotations in 3D and their computational validation. *Z. Angew. Math. Mech.*, 97(7):843–871, 2017. 3, 4, 5, 8, 11, 13, 18, 24
- [14] G. Grioli. Una proprietà di minimo nella cinematica delle deformazioni finite. *Boll. Un. Math. Ital.*, 2:252–255, 1940. 3
- [15] N. J. Higham. Computing the nearest symmetric positive semi-definite matrix. *Lin. Algebra Appl.*, 103:103–118, 1988. 7, 10, 27
- [16] J. Jeong, H. Ramézani, I. Münch, and P. Neff. A numerical study for linear isotropic Cosserat elasticity with conformally invariant curvature. *Z. Angew. Math. Mech.*, 89(7):552–569, 2009. 2
- [17] P. J. Konijnenberg, S. Zaefferer, and D. Raabe. Assessment of geometrically necessary dislocation levels derived by 3D-EBSD. *Acta Mater.*, 99:402 – 414, 2015. 12
- [18] J. Konrad, S. Zaefferer, and D. Raabe. Investigation of orientation gradients around a hard Laves particle in a warm-rolled Fe3Al-based alloy using a 3D EBSD-FIB technique. *Acta Mater.*, 54(5):1369 – 1380, 2006. 12
- [19] J. Lankeit, P. Neff, and Y. Nakatsukasa. The minimization of matrix logarithms: On a fundamental property of the unitary polar factor. *Lin. Alg. Appl.*, 449:28–42, 2014. 4, 20
- [20] J. M. Lee. *Introduction to Smooth Manifolds*. Graduate Texts in Mathematics. Springer, 2002. 18
- [21] A. Ma. *Modeling the constitutive behavior of polycrystalline metals based on dislocation mechanisms*. PhD thesis, RWTH Aachen, 2006. 12, 13, 21, 24
- [22] A. Ma and F. Roters. A constitutive model for fcc single crystals based on dislocation densities and its application to uniaxial compression of aluminium single crystals. *Acta Mater.*, 52(12):3603 – 3612, 2004. 12, 13, 21, 24
- [23] L. C. Martins and P. Podio-Guidugli. An elementary proof of the polar decomposition theorem. *Amer. Math. Month.*, 87:288–290, 1980. 3
- [24] G. A. Maugin. On the structure of the theory of polar elasticity. *R. Soc. Lond. Philos. Trans. Ser. A Math. Phys. Eng. Sci.*, 356(1741):1367–1395, 1998. 2
- [25] I. Münch and P. Neff. A nonlinear micropolar continuum theory for initial plasticity. In A. Zigoni, editor, *Advances and Trends in Structural Engineering, Mechanics and Computation.*, pages 269–272. CRC Press/Balkema, ISBN 978-0-415-58472-2, 2010. 9
- [26] P. Neff. *Geometrically exact Cosserat theory for bulk behaviour and thin structures. Modelling and mathematical analysis*. Signatur HS 7/0973. Habilitationsschrift, Universitäts- und Landesbibliothek, Technische Universität Darmstadt, Darmstadt, 2004. 8, 24

- [27] P. Neff. The Cosserat couple modulus for continuous solids is zero viz the linearized Cauchy-stress tensor is symmetric. *Z. Angew. Math. Mech.*, 86:892–912, 2006. 11, 13
- [28] P. Neff. A finite-strain elastic-plastic Cosserat theory for polycrystals with grain rotations. *Int. J. Engng. Sci.*, 44:574–594, 2006. 8
- [29] P. Neff. Remarks on invariant modelling in finite strain gradient plasticity. *Techn. Mech.*, 28(1):13–21, 2008. 8, 10
- [30] P. Neff, K. Chelminski, and H.-D. Alber. Notes on strain gradient plasticity: Finite strain covariant modelling and global existence in the infinitesimal rate-independent case. *Math. Mod. Meth. Appl. S.*, 19(02):307–346, 2009. 8, 10
- [31] P. Neff, B. Eidel, and R. J. Martin. Geometry of logarithmic strain measures in solid mechanics. *Arch. Rat. Mech. Anal.*, 222(2):507–572, Nov 2016. 9
- [32] P. Neff, B. Eidel, F. Osterbrink, and R. Martin. A Riemannian approach to strain measures in nonlinear elasticity. *C. R. Acad. Sci. Paris (Mecanique)*, 342(4):254–257, 2014. 9
- [33] P. Neff, A. Fischle, and I. Münch. Symmetric Cauchy-stresses do not imply symmetric Biot-strains in weak formulations of isotropic hyperelasticity with rotational degrees of freedom. *Acta Mech.*, 197:19–30, 2008. 13, 24
- [34] P. Neff and J. Jeong. A new paradigm: the linear isotropic Cosserat model with conformally invariant curvature energy. *Z. Angew. Math. Mech.*, 89(2):107–122, 2009. 2
- [35] P. Neff, J. Jeong, and A. Fischle. Stable identification of linear isotropic Cosserat parameters: bounded stiffness in bending and torsion implies conformal invariance of curvature. *Acta Mech.*, 211(3-4):237–249, 2010. 2
- [36] P. Neff, J. Lankeit, and A. Madeo. On Grioli’s minimum property and its relation to Cauchy’s polar decomposition. *Int. J. Engng. Sci.*, 80:209–217, 2014. 3, 4
- [37] P. Neff and I. Münch. Curl bounds Grad on $SO(3)$. *ESAIM: COCV*, 14(1):148–159, 2008. 9, 10
- [38] P. Neff and I. Münch. Simple shear in nonlinear Cosserat elasticity: bifurcation and induced microstructure. *Cont. Mech. Thermod.*, 21(3):195–221, 2009. 11, 12
- [39] P. Neff, Y. Nakatsukasa, and A. Fischle. A logarithmic minimization property of the unitary polar factor in the spectral and Frobenius norms. *SIAM J. Matrix Anal. Appl.*, 35(3):1132–1154, 2014. 4, 20
- [40] E. Orowan. Zur Kristallplastizität. III. Über den Mechanismus des Gleitvorganges (To crystal plasticity. III. About the mechanism of glide). *Z. Phys.*, 89(9):634–659. 9
- [41] M. Polanyi. Über eine Art Gitterstörung, die einen Kristall plastisch machen könnte (About a kind of lattice distortion that could render a crystal plastic (= ductile)). *Z. Phys.*, 89(9):660–664. 9
- [42] V. L. Popov and S. G. Psakhie. Theoretical principles of modelling elastoplastic media by moveable cellular automata method. I: Homogenous media. *Phys. Mesomechanics*, 4(15):16–25, 2001. 19
- [43] V. Randle and O. Engler. *Introduction to texture analysis: macrotexture, microtexture and orientation mapping*. CRC Press, 2nd edition, 2000. 14, 20
- [44] F. Roters, P. Eisenlohr, L. Hantcherli, D. D. Tjahjanto, T.R. Bieler, and D. Raabe. Overview of constitutive laws, kinematics, homogenization and multiscale methods in crystal plasticity finite-element modeling: Theory, experiments, applications. *Acta Mater.*, 58(4):1152 – 1211, 2010. 13
- [45] S. Sadik and A. Yavari. On the origins of the idea of the multiplicative decomposition of the deformation gradient. *Math. Mech. Solids*, 22(4):771–772, 2017. 8
- [46] D. Serre. *Matrices: Theory and Applications*. Graduate Texts in Mathematics. Springer, 2002. 4
- [47] A. Y. Smolin, G. M. Eremina, E. V. Shilko, and S. G. Psakhie. Study of the role of vortex displacement in contact loading of strengthening coatings based on movable cellular automaton modeling. *AIP Conference Proceedings*, 1683, 2015. 19
- [48] G. I. Taylor. The mechanism of plastic deformation of crystals. Part I. Theoretical. *P. Roy. Soc. Lond. A*, 145(855):362–387, 1934. 9
- [49] G. I. Taylor. The mechanism of plastic deformation of crystals. Part II. Comparison with observations. *P. Roy. Soc. Lond. A*, 145(855):388–404, 1934. 9
- [50] Y. Wang, D. Raabe, C. Klüber, and F. Roters. Orientation dependence of nanoindentation pile-up patterns and of nanoindentation microtextures in copper single crystals. *Acta Mater.*, Volume 52:2229–2238, 2004. 16
- [51] N. Zaafarani. *Experimental and theoretical investigation of nanoindentation in a Cu crystal*. PhD thesis, Faculty of Georesources and Materials Engineering, RWTH Aachen, 2008. 7, 12, 13, 14, 21, 24
- [52] N. Zaafarani, D. Raabe, F. Roters, and S. Zaeferrer. On the origin of deformation-induced rotation patterns below nanoindenters. *Acta Mater.*, 56(1):31 – 42, 2008. 7, 13, 24
- [53] N. Zaafarani, N. Raabe, R. N. Singh, F. Roters, and S. Zaeferrer. Three-dimensional investigation of the texture and microstructure below a nanoindent in a Cu single crystal using 3D EBSD and crystal plasticity finite element simulations. *Acta Mater.*, Volume 54/7:1863–1876, 2006. <http://www.sciencedirect.com/science/article/B6TW8-4J91NNJ-1/2/76ab02ad11c9d01d545627eeb5df081b>. 7, 12, 13, 14, 16, 21, 22, 23, 24
- [54] S. Zaeferrer, S.I. Wright, and D. Raabe. Three-dimensional orientation microscopy in a focused ion beam–scanning electron microscope: A new dimension of microstructure characterization. *Metall. Mater. Trans. A*, 39(2):374–389, 2008. 12, 13
- [55] C. Zambaldi and D. Raabe. Plastic anisotropy of γ -TiAl revealed by axisymmetric indentation. *Acta Mater.*, 58(9):3516 – 3530, 2010. 16
- [56] C. Zambaldi, Y. Yang, T. R. Bieler, and D. Raabe. Orientation informed nanoindentation of α -titanium: Indentation pileup in hexagonal metals deforming by prismatic slip. *J. Mater. Res.*, 27:356–367, 1 2012. 16
- [57] C. Zambaldi, C. Zehnder, and D. Raabe. Orientation dependent deformation by slip and twinning in magnesium during single crystal indentation. *Acta Mater.*, 91:267 – 288, 2015. 16

A Supplementary Material

A.1 Best-approximation in $\text{Sym}^+(3)$ (due to Higham)

First, we provide a short exposition of Higham's best approximation of a given matrix $X \in \mathbb{R}^{3 \times 3}$ in the closed cone of symmetric positive semi-definite matrices $\overline{\text{Sym}^+(3)}$.

Theorem A.1 (Higham's approximation theorem [15]). *Let $X \in \mathbb{R}^{3 \times 3}$ and let*

$$\pi(X) := \arg \inf_{S \in \text{Sym}^+(3)} \|X - S\| \quad (1.1)$$

denote the mapping of X to its best approximation in $\overline{\text{Sym}^+(3)}$ with respect to the Frobenius matrix norm. Then there exists a unique best approximation $\pi(X) = P \in \text{Sym}^+(3)$ of the explicit form

$$\pi(X) = \frac{1}{2} (\text{sym}(X) + Z) . \quad (1.2)$$

Here $Z \in \overline{\text{Sym}^+(3)}$ is the symmetric factor of the polar decomposition $\text{sym}(X) = QZ$, $Q \in \text{O}(3)$.

Corollary A.2 (The symmetric positive definite case). *If the symmetric part $\text{sym}(X)$ is positive definite, then*

$$\pi(X) = \text{sym}(X) . \quad (1.3)$$

Proof. We apply Higham's approximation theorem. First we compute the right polar decomposition of $\text{sym}(X) = QZ$ which yields the symmetric factor $Z \in \text{Sym}(3)$. Similar to the usual computation of the stretch tensor, we find

$$Z = \sqrt{\text{sym}(X)^T \text{sym}(X)} = \sqrt{\text{sym}(X)^2} . \quad (1.4)$$

By assumption $\text{sym}(X)$ is symmetric positive definite. Thus, since the symmetric positive definite matrix square root is unique, we obtain

$$Z = \sqrt{\text{sym}(X)^2} = \text{sym}(X) . \quad (1.5)$$

This shows that the best approximation of X is given by

$$\pi(X) = \frac{1}{2} (\text{sym}(X) + \text{sym}(X)) = \text{sym}(X) \in \text{Sym}^+(3) . \quad \blacksquare$$

Next, we present a simple condition which implies the positive definiteness of $\text{sym}(X)$. Note first that

$$\langle \text{sym}(X)\xi, \xi \rangle = \langle X\xi, \xi \rangle > 0 \iff \langle (X - \mathbf{1} + \mathbf{1})\xi, \xi \rangle = \underbrace{\langle \text{sym}(X - \mathbf{1})\xi, \xi \rangle + \|\xi\|^2}_{\text{A}} > 0 . \quad (1.6)$$

Since

$$\langle (X - \mathbf{1})\xi, \xi \rangle = \langle \text{sym}(X - \mathbf{1})\xi, \xi \rangle \leq \|\text{sym}(X - \mathbf{1})\| \|\xi\|^2 , \quad (1.7)$$

we observe that

$$\langle \text{sym}(X)\xi, \xi \rangle = \text{A} \geq \|\xi\|^2 - \|\text{sym}(X - \mathbf{1})\| \|\xi\|^2 = (1 - \|\text{sym}(X - \mathbf{1})\|) \|\xi\|^2 . \quad (1.8)$$

We conclude that $\text{sym}(X)$ is positive definite if $\|\text{sym}(X - \mathbf{1})\| < 1$. Moreover, the inequality $\|\text{sym}(X - \mathbf{1})\| \leq \|X - \mathbf{1}\|$ shows that $\text{sym}(X)$ is positive definite if $\|X - \mathbf{1}\| < 1$.

A.2 Algorithmic implementation of $\text{rpolar}_{1,0}^{\pm}(F)$

For our computations, we have used the following implementation of $\text{rpolar}_{1,0}^{\pm Q}(F)$ in **Mathematica**:

```
(* Right polar decomposition of the deformation gradient F*)
PolarDecomposition[F_] := Module[{PolarF, U},
  U = MatrixPower[Transpose[F].F, 1/2];
  PolarF = F.Inverse[U];
  {PolarF, U};
];

(* Relaxed polar factors  $\text{rpolar}_{1,0}^{\pm}(F)$  of the deformation gradient F *)
RelaxedPolarDecomposition[F_] :=
Module[{Q, Spec, RHat, alphaHat, PolarF, RPolarPlus, RPolarMinus},

  {PolarF, U} = PolarDecomposition[F],
  (* The columns of Q are the eigenvectors of U in the canonical basis *)
  Q = Transpose[Map[#, Sqrt[#. #]] &, Eigenvectors[U]];

  (* Enforce (nearly) consistent orientation of orthonormal eigenframe:
  this is a specific solution for the presented synthetic nanoindentation. *)
  If[Det[Q] < 0,
```

```

Q[[All, 3]] = -Q[[All, 3]];
];

(* Singular value spectrum of F / Eigenvalues of U ordered by decreasing magnitude *)
Spec = Eigenvalues[U];

(* Maximal mean planar strain *)
S_MMP = 1/2*(Spec[[1]] + Spec[[2]]);

(* Compute relative rotation angle for  $\mu = 1$  and  $\mu_c = 0$  *)
If[S_MMP > 1, alphaHat = ArcCos[1/S_MMP], alphaHat = 0];

(* Parametrize relative rotation  $\hat{R}$  in plane of maximal stretch *)
RHat[alphaHat_] := {{Cos[alphaHat], -Sin[alphaHat], 0},
                   {Sin[alphaHat], Cos[alphaHat], 0},
                   {0, 0, 1}};

(* Positive branch relative to a choice of orientation for Q *)
RPolarPlus = PolarF.Q.RHat[-alphaHat].Transpose[Q];

(* Negative branch relative to a choice of orientation for Q *)
RPolarMinus = PolarF.Q.RHat[alphaHat].Transpose[Q];

(* Return both branches *)
{RPolarPlus, RPolarMinus}
];

```